Reconciling Assumptions in Bottom-up and Top-down Approaches for Estimating Aerosol Emission Rates from Wildland Fires using Observations from FIREX-AQ

Elizabeth Brooke Wiggins[1], Bruce Anderson[1], Matthew Brown[1], Pedro Campuzano-Jost[2], Gao Chen[1], James Crawford[1], Ewan Crosbie[1], Jack Dibb[3], Joshua Digangi[1], Glenn Diskin[1], Marta Fenn[1], Francesca Gallo[4], Emily Gargulinski[5], Hongyu Guo[2], John Hair[1], Hannah Halliday[6], Charles Ichoku[7], Jose Jimenez[2], Carolyn Jordan[1], Joseph Katich[2], John Nowak[1], Anne Perring[8], Claire Robinson[1], Kevin Sanchez[4], Melinda Schueneman[2], Joshua Schwarz[9], Taylor Shingler[1], Michael Shook[1], Amber Soja[1], Chelsea Stockwell[2], Kenneth Thornhill[1], Katherine Travis[1], Carsten Warneke[9], Edward Winstead[1], Luke Ziemba[1], and Richard Moore[1]

[1]NASA Langley Research Center
[2]CIRES
[3]University of New Hampshire
[4]NASA Postdoctoral Program
[5]National Institute of Aerospace
[6]Environmental Protection Agency
[7]Howard University
[8]Colgate University
[9]NOAA Chemical Science Laboratory

November 24, 2022

Abstract

Accurate fire emissions inventories are crucial to predict the impacts of wildland fires on air quality and atmospheric composition. Two traditional approaches are widely used to calculate fire emissions: a satellite-based top-down approach and a fuels-based bottom-up approach. However, these methods often considerably disagree on the amount of particulate mass emitted from fires. Previously available observational datasets tended to be sparse, and lacked the statistics needed to resolve these methodological discrepancies. Here, we leverage the extensive and comprehensive airborne in situ and remote sensing measurements of smoke plumes from the recent Fire Influence on Regional to Global Environments and Air Quality (FIREX-AQ) campaign to statistically assess the skill of the two traditional approaches. We use detailed campaign observations to calculate and compare emission rates at an exceptionally high resolution using three separate approaches: top-down, bottom-up, and a novel approach based entirely on integrated airborne in situ measurements. We then compute the daily average of these high-resolution estimates and compare with estimates from lower resolution, global top-down and bottom-up inventories. We uncover strong, linear relationships between all of the high-resolution emission rate estimates in aggregate, however no single approach is capable of capturing the emission characteristics of every fire. Global inventory emission rate estimates exhibited weaker correlations with the high-resolution approaches and displayed evidence of systematic bias. The disparity between the low resolution global inventories and the high resolution approaches is likely caused by high levels of uncertainty in essential variables used in bottom-up inventories and imperfect assumptions in top-down inventories.

Hosted file

`essoar.10507773.1.docx` available at https://authorea.com/users/523143/articles/604107-reconciling-assumptions-in-bottom-up-and-top-down-approaches-for-estimating-aerosol-emission-rates-from-wildland-fires-using-observations-from-firex-aq

1 **Reconciling Assumptions in Bottom-up and Top-down Approaches for Estimating**
2 **Aerosol Emission Rates from Wildland Fires using Observations from FIREX-AQ**

3 **E. B. Wiggins[1,2], B. E. Anderson[2], M. D. Brown[2,3], P. Campuzano-Jost[4], G. Chen[2], J.**
4 **Crawford[2], E. C. Crosbie[2,3], J. Dibb[5], J. P. DiGangi[2], G. S. Diskin[2], M. Fenn[2,3], F. Gallo[1,2],**
5 **E. Gargulinski[6], H. Guo[4], J. W. Hair[2], H. S. Halliday[7], C. Ichoku[8], J. L. Jimenez[4], C. E.**
6 **Jordan[2,6], J. M. Katich[4,9], J. B. Nowak[2], A. E. Perring[10], C. E. Robinson[2,3], K. J.**
7 **Sanchez[1,2], M. Schueneman[4], J. P. Schwarz[9], T. J. Shingler[2], M. A. Shook[2], A. Soja[2,6], C. E.**
8 **Stockwell[4,9], K. L. Thornhill[2,3], K. R. Travis[2], C. Warneke[9], E. L. Winstead[2,3], L. D.**
9 **Ziemba[2], and R. H. Moore[2]**

10 [1]NASA Postdoctoral Program, Universities Space Research Association, Columbia, MD

11 [2]NASA Langley Research Center, Hampton, VA

12 [3]Science Systems and Applications, Inc., Hampton, VA

13 [4]CIRES, University of Colorado Boulder, Boulder, CO, USA

14 [5]Earth Systems Research Center, University of New Hampshire, NH, USA

15 [6]National Institute of Aerospace, Hampton, VA

16 [7]Environmental Protection Agency, Research Triangle, NC, USA

17 [8]College of Arts and Sciences, Howard University, Washington, DC, USA

18 [9]NOAA Chemical Science Laboratory, Boulder, CO, USA

19 [10]Department of Chemistry, Colgate University, Hamilton, NY, USA

20 Corresponding authors: Elizabeth B. Wiggins (elizabeth.b.wiggins@nasa.gov) and Richard H.
21 Moore (richard.h.moore@nasa.gov)

22 **Key Points:**

23 • In situ measurements of wildland fire smoke plumes provide emission rates for
24   evaluating emissions inventories at unprecedented resolution

25 • Fire emissions inventories struggle to capture the emissions rate characteristics of
26   individual fires but may perform well in the aggregate

27 • Bottom-up inventories suffer from major uncertainty in key variables, while top-down
28   inventories may have bias from imperfect assumptions
29

30   **Abstract**

31   Accurate fire emissions inventories are crucial to predict the impacts of wildland fires on air
32   quality and atmospheric composition. Two traditional approaches are widely used to calculate
33   fire emissions: a satellite-based top-down approach and a fuels-based bottom-up approach.
34   However, these methods often considerably disagree on the amount of particulate mass emitted
35   from fires. Previously available observational datasets tended to be sparse, and lacked the
36   statistics needed to resolve these methodological discrepancies. Here, we leverage the extensive
37   and comprehensive airborne in situ and remote sensing measurements of smoke plumes from the
38   recent Fire Influence on Regional to Global Environments and Air Quality (FIREX-AQ)
39   campaign to statistically assess the skill of the two traditional approaches. We use detailed
40   campaign observations to calculate and compare emission rates at an exceptionally high
41   resolution using three separate approaches: top-down, bottom-up, and a novel approach based
42   entirely on integrated airborne in situ measurements. We then compute the daily average of these
43   high-resolution estimates and compare with estimates from lower resolution, global top-down
44   and bottom-up inventories. We uncover strong, linear relationships between all of the high-
45   resolution emission rate estimates in aggregate, however no single approach is capable of
46   capturing the emission characteristics of every fire. Global inventory emission rate estimates
47   exhibited weaker correlations with the high-resolution approaches and displayed evidence of
48   systematic bias. The disparity between the low resolution global inventories and the high
49   resolution approaches is likely caused by high levels of uncertainty in essential variables used in
50   bottom-up inventories and imperfect assumptions in top-down inventories.

51   **Plain Language Summary**

52   Smoke emitted by wildland fires is dangerous to human health and contributes to climate change.
53   To predict and evaluate the impacts of fires, we need to know how much smoke is emitted into
54   the atmosphere. There are two state-of-the-art methods used to estimate the mass of smoke
55   emitted by fires, but they often disagree. In this study, we use unusually detailed measurements
56   collected using an aircraft that flew within wildland fire smoke plumes to calculate the amount of
57   smoke emitted from fires in the Western United States. We compare emission rates derived from
58   the exceptionally high spatial and temporal resolution approach to the two traditional, lower
59   resolution approaches to understand why they sometimes diverge.

60   **1 Introduction**

61   Wildland fires can be dangerous, destructive forces of nature that degrade air quality and
62   threaten human health and infrastructure (Larsen et al., 2018). However, fires are also a naturally
63   occurring disturbance needed to maintain the health and biodiversity of many ecosystems
64   (Goldammer et al., 2008; Weaver, 1974). In the Western United States, the natural fire cycle has
65   been completely disrupted and distorted by human interference (Fusco et al., 2016; Harvey,
66   2016), where large increases in fire size and occurrence are transpiring because of a buildup of
67   fuels caused by historically excessive fire suppression, increased settlement in the wildland
68   urban interface, and more favorable fire weather conditions (Abatzoglou & Williams, 2016;
69   Dennison et al., 2014; Mell et al., 2010; Stavros et al., 2014; Stephens & Ruth, 2005; Theobald
70   & Romme, 2007; Westerling et al., 2003). There is a need for balance between reducing the

71 hazards of wildland fires while maintaining forest health under the influence of a changing
72 climate.
73   Unless we can better understand and predict the deleterious impacts of wildland fire
74 smoke emissions on air quality and human health, it will be nearly impossible for society to
75 respond and adapt to this evolving and complex system. Informed land management policy that
76 utilizes prescribed fires to reduce fuel buildup and reinvigorate ecosystems in order to ultimately
77 minimize smoke exposure for downwind communities necessitates the ability to quantify the
78 composition, magnitude, and transport of smoke (Noss et al., 2006; Schweizer et al., 2018). In
79 the case of accidental or uncontrolled wildfires, the capability to accurately predict smoke
80 transport is necessary to alert sensitive populations and mitigate the overall impact of smoke on
81 human health (Larkin et al., 2009; McKenzie et al., 2006). Atmospheric models rely entirely on
82 geospatial databases of fire locations and estimated emissions (so-called fire emissions
83 inventories) to represent the contribution of fire emissions to downwind atmospheric
84 composition (Wiedinmyer et al., 2006). Two distinct approaches are traditionally used to create
85 these emissions inventories: a fuels-based bottom-up approach and a satellite-based top-down
86 approach (Seiler & Crutzen, 1980; Wooster et al., 2005).
87   The bottom-up approach calculates the mass of carbon emitted by a fire as the product of
88 burned area, fuel mass per unit area, the carbon fraction of fuel, and combustion completeness
89 (Seiler & Crutzen, 1980). This approach, also known as the carbon mass balance method,
90 operates under the explicit assumption that all burnt biomass carbon is volatilized and emitted to
91 the atmosphere (Ward & Radke, 1993). Although a fuels-based approach is the key feature of
92 bottom-up algorithms, most also rely on remote sensing observations from satellite sensors such
93 as the Moderate Resolution Imaging Spectroradiometer (MODIS) or Visible Infrared Imaging
94 Radiometer Suite (VIIRS) to determine burned area. Burned area can be calculated using active
95 fire detections, by assuming the entire landscape captured in the resolution of a single satellite
96 pixel burned, or burned area can be taken directly from higher level data products (Kaiser et al.,
97 2012; van der Werf et al., 2017; Wiedinmyer et al., 2011). Fuel mass per unit area is often
98 derived from either a biogeochemical model initialized with satellite observations and/or from
99 labor intensive fuel databases of fuel type and loading (McKenzie et al., 2012; Pettinari &
100 Chuvieco, 2016; Sandberg et al., 2001; van der Werf et al., 2017). Fuel carbon content is often
101 assumed based on laboratory measurements from previous studies or estimated using the sum of
102 CO_2, CO, and CH_4 emission factors (Akagi et al., 2011; McMeeking et al., 2009; Santín et al.,
103 2015; Susott et al., 1991; van der Werf et al., 2017; Yokelson et al., 1997). Combustion
104 completeness is calculated as a function of changes in visual landscape characteristics, reduction
105 in fuel moisture, increase in summer land surface temperature, tree cover, and/or daily fire
106 weather indices (Kaiser et al., 2012; van der Werf et al., 2017; Wiedinmyer et al., 2011).
107   The bottom-up approach requires an ecosystem-specific emission factor to convert total
108 carbon mass emissions to emissions of a particular trace gas or aerosol species (Akagi et al.,
109 2011; Andreae & Merlet, 2001). Emission factors are often attained from compilations of
110 previous studies categorized by fuel or vegetation type and show a wide range of natural
111 variability depending on the exact composition of fuel being burned and combustion conditions.
112 Certain species, including many volatile organic compounds (VOCs) and aerosols, rapidly
113 evolve in the atmosphere following emission, which necessitates emission factor estimates
114 derived only from measurements of young, fresh smoke. There are numerous particulate mass
115 (PM) emission factors published from ground and laboratory based studies, however in situ

116 airborne measurements of PM emission factors for Western US wildland fires are particularly
117 scarce (Akagi et al., 2011).
118   The top-down approach follows from Wooster et al. (2005), who showed that the burning
119 of dry vegetation yields the same amount of energy, regardless of fuel type. Top-down
120 inventories assume fire radiative power (FRP) observations from satellite remote sensing can be
121 used as a direct measurement of the amount of biomass consumed in a fire in an effort to bypass
122 the latency and uncertainty associated with variables required in bottom-up style inventories
123 (Ichoku & Kaufman, 2005). In the top-down approach, FRP is multiplied by a predetermined
124 coefficient, known as a smoke emission coefficient (C_e), to calculate fire emission rates of PM.
125 Smoke emission coefficients are constants derived for individual ecosystems by combining
126 multiple years of aerosol optical depth (AOD) remote sensing observations with a mass
127 extinction efficiency (MEE), a constant that relates particle extinction to particle mass (Giglio et
128 al., 2006; Ichoku et al., 2008; Kaiser et al., 2012). Ichoku et al. (2008) demonstrated that the
129 relationship between fire radiative energy (FRE), or temporally integrated FRP, and the emission
130 rate of PM could be quantified using AOD during a controlled laboratory-based experiment. The
131 smoke emission coefficient determined from the laboratory-based experiment agrees with
132 independent estimates derived from satellite measurements of FRP and AOD measured over
133 large-scale wildfires, which leads to the assumption that this approach can be extrapolated to
134 global scale observations of FRP and AOD.
135   There are dozens of top-down and bottom-up emissions inventories available for use in
136 atmospheric transport models. These inventories encompass wide ranges of spatial and temporal
137 scales and can be used to account for hundreds of individual pollutants emitted by fires
138 (Darmenov & da Silva, 2013; Ichoku & Ellison, 2014; Kaiser et al., 2009; Mota & Wooster,
139 2018; van der Werf et al., 2017; Wiedinmyer et al., 2011). The choice of which inventory to use
140 in modeling applications is crucial, because different fire emissions inventories can profoundly
141 disagree on the magnitude, composition, and temporal variability of fire emissions, especially
142 PM (Carter et al., 2020; Larkin et al., 2014; Liu et al., 2020; Pan et al., 2020). The underlying
143 cause of the disagreement is difficult to isolate, but could be an artifact of the various
144 assumptions used in each inventory. Most global emissions inventories are plagued with high
145 levels of uncertainty stemming from the individual datasets used to calculate emissions, which
146 further complicates the ability to isolate the cause of the discrepancies among inventories
147 (French et al., 2004; Urbanski et al., 2011; Wiedinmyer et al., 2011). For example, the detection
148 and quantification of active fire locations, FRP, and AOD using satellite remote sensing suffers
149 from the obscuration of the land surface by clouds or thick smoke, limited spatiotemporal
150 coverage or resolution, and instrument detection limits.
151   It is fundamentally challenging to correctly quantify biomass burning emissions due to
152 the highly variable composition and structure of the fuels that fires consume, and because fires
153 can rapidly change their behavior in response to dynamic meteorological or environmental
154 conditions (Kennedy et al., 2020; Liu, 2004; Schultz et al., 2008). The datasets used in global fire
155 emissions inventories attempt to capture these dynamics, but they often lack the spatial and
156 temporal resolution needed to fully encapsulate all of the individual components that influence
157 emissions. Intensive in situ measurements of smoke from the joint NASA/NOAA Fire Influence
158 on Regional to Global Environments and Air Quality (FIREX-AQ) campaign that was conducted
159 during the summer of 2019 provide a unique opportunity to evaluate the assumptions and
160 uncertainties in both top-down and bottom-up approaches for calculating fire emissions. During
161 FIREX-AQ, the NASA DC-8 aircraft was outfitted with a comprehensive instrument payload

162 that sampled smoke plumes from Western US wildland fires and Southeastern US prescribed and
163 agricultural fires. The plume sampling strategy for the western portion of the campaign consisted
164 of an above-plume, longitudinal run along the entire length of the plume to allow for nadir-
165 pointing remote sensing of the smoke followed by a set of plume transects perpendicular to the
166 direction of smoke transport where the aircraft sampled the plume in situ during a series of
167 sequentially-downwind, cross-sectional passes (Wiggins et al., 2020).
168   Measurements collected during FIREX-AQ provide the opportunity for a rare direct
169 comparison and evaluation of the traditional, lower resolution approaches to calculate fire
170 emissions at an unusually high spatial and temporal resolution. In this study, we calculate fire
171 total carbon and total PM emission rates from Western US wildland fires sampled during
172 FIREX-AQ using a novel, independent approach based on in situ smoke plume measurements.
173 Here, we integrate in situ trace gas and aerosol measurements with information on plume
174 thickness gleaned from airborne High-Spectral Resolution Lidar (HSRL) measurements to
175 calculate emission rates. Although this new approach is subject to its own uncertainties and
176 sources of error, we assume emission rate estimates derived from this approach are as close to
177 accurate as we can realistically achieve, because they are based on in situ measurements, and
178 their calculation doesn't require as many strong assumptions as the more traditional approaches.
179 We further capitalize on FIREX-AQ data to calculate fire emission rates using a high-resolution
180 top-down approach and a high-resolution bottom-up approach. The high-resolution top-down
181 approach (referred to as HSRL-GOES) uses airborne HSRL measurements of particle extinction
182 instead of satellite observations of AOD, and the high-resolution bottom-up approach (referred to
183 as Fuel2Fire) uses carbon emission estimates from the newly-developed Fuel2Fire carbon
184 emissions inventory that has been developed and optimized specifically to estimate emissions
185 from the fires sampled during FIREX-AQ. We also obtain emission rates from a traditional
186 bottom-up fire emissions inventory, Global Fire Emissions Database (GFED4.1s), and a
187 traditional top-down fire emissions inventory, Fire Energetics and Emissions Research
188 (FEERv1.0). GFED and FEER have much lower temporal and spatial resolutions (3-hr/daily,
189 0.25° and daily, 0.1° respectively) compared to the three high-resolution FIREX-AQ based
190 approaches. We evaluate the performance of GFED and FEER, along with the high-resolution
191 approaches, against the in situ measurement based approach to investigate potential bias and
192 assess the validity of the assumptions unique to each approach (Figure 1). We also investigate
193 and quantify uncertainty for all of the approaches used to calculate emission rates in this study.
194 The goal of this paper is to understand how the estimates of total carbon and PM emission rates
195 from traditional, lower resolution methods compare to the high-resolution estimates available for
196 the fires sampled during the FIREX-AQ campaign. The results of this analysis should be of keen
197 interest for the global wildfire emissions inventory community as well as atmospheric scientists
198 seeking to use airborne observations to constrain wildland fire aerosol emissions.

199 **2 Methods**

200 **2.1 Emission Rate Estimates from Global Inventories**

201   **2.1.1 GFED4.1s (Low-Resolution Bottom-up)**

202   GFED is a global fire emissions inventory that internally calculates carbon emission rates
203 using a traditional bottom-up approach as follows

204
$$E_C = BA \times FL \times CC \times F_C \tag{1}$$

205 where E_C is the carbon mass emission rate, BA is the burned area, FL is the fuel mass loading
206 per area, CC is the combustion completeness (expressed as a percent), and F_C is the mass fraction
207 of carbon in the fuel (van der Werf et al., 2017). GFED obtains burned area estimates from
208 MODIS (MCD64A1), fuel loading and combustion completeness are derived from the Carnegie-
209 Ames-Stanford Approach (CASA) biogeochemical model, and carbon mass fraction is defined
210 per ecosystem from compilations of previous studies (Akagi et al., 2011; Andreae & Merlet,
211 2001; van der Werf et al., 2017).
212   To represent a traditional bottom-up approach, we use daily average carbon emission
213 rates per area from GFED4.1s (https://www.globalfiredata.org/) to calculate daily average PM
214 emission rates (E_{PM}) for the western fires sampled during FIREX-AQ as follows

215
$$E_{PM} = EF_{PM} \times \sum \frac{\hat{E}_C \times A_{P,GFED}}{F_c} \tag{2}$$

216 where EF_{PM} is the total particulate matter mass emission factor suggested by GFED for
217 temperate forests (17.6 gPM kg-biomass consumed^{-1}), $\hat{E}_C$ is the area-normalized daily carbon
218 emissions in each GFED pixel, $A_{P,GFED}$ is the GFED pixel area (0.25° x 0.25°), and the
219 summation is carried out over all GFED pixels within 0.25° of the centroid of the final United
220 States Geological Survey Geospatial Multi-Agency Coordination (GeoMAC) fire perimeter for
221 each fire. In Equation 2, we use the F_C suggested by GFED for temperate forests (0.489 kgC kg-
222 biomass consumed^{-1}). The use of ecosystem level constant values for EF_{PM} and F_C is intended to
223 provide good results in aggregate on the regional-to-global scales required by models, although
224 individual fires will deviate from these specifications. GFED data is provided on a daily and a 3-
225 hr basis in UTC time, and here we use the daily product. We convert from UTC time to local
226 time by assuming daily emissions (local time) are equal to 75% of the emissions from the day a
227 given fire was sampled by the DC-8 aircraft (local time) plus 25% of the emissions from the day
228 after (local time).
229   We estimate relative uncertainty in E_C and E_{PM} estimates derived from GFED by
230 propagating uncertainty through equation 1 and equation 2. For equation 1, we assume the
231 following relative uncertainties: BA = 44%, FL = 111%, CC = 11%, and F_C = 10%. For equation
232 2, we assume EF_{PM} has a relative uncertainty of 36% and E_C has a relative uncertainty calculated
233 by propagating uncertainty through equation 1. We obtain the relative uncertainty in the BA
234 product used by GFED from an analysis of MODIS burned area by Giglio et al. (2018). FL and
235 CC relative uncertainty are derived by taking the standard deviation divided by the average for
236 all field measurements of Western US fuels as compiled by van Leeuwen et al. (2014) and
237 updated by van der Werf et al. (2017). F_C relative uncertainty is defined as the standard deviation
238 divided by the average in F_C values given by Akagi et al. (2011). The relative uncertainty in
239 EF_{PM} is calculated as the standard deviation divided by the average of EF_{PM} derived from all
240 previous studies of temperate forest EF_{PM} measurements used in GFED (Akagi et al., 2011;

241 Andreae and Merlet, 2001; van der Werf et al. 2017). The calculated relative uncertainty in
242 GFED E_{PM} is 126% and E_C is 120% (Supplementary Table S1).

2.1.2 FEERv1.0 (Low-Resolution Top-down)

244 FEER is a global fire emissions inventory that calculates daily average E_{PM} using a
245 traditional top-down approach as

$$E_{PM} = C_e \times FRP \tag{3}$$

247 where C_e is an ecosystem-dependent predetermined smoke emission coefficient, and FRP
248 observations are from MODIS. FEER derives C_e using multiple years of coupled MODIS AOD
249 at 550nm and FRP observations and an assumed constant MEE at 550nm of 4.6 m^2 g^{-1} derived
250 from previous studies (Reid et al., 2005b). Smoke emission coefficients have been predetermined
251 by FEER and are provided globally at a 1° x 1° resolution
252 (https://feer.gsfc.nasa.gov/projects/emissions/) (Ichoku & Ellison, 2014).
253 Daily average E_{PM} estimates are provided at a 0.1° x 0.1° resolution through a coupling
254 of FEER smoke emission coefficients and MODIS FRP observations (FEERv1.0-G1.2). For the
255 traditional top-down approach, we calculate daily average E_{PM} estimates for each of the western
256 fires sampled during FIREX-AQ as

$$E_{PM} = \sum \widehat{E}_{PM_{FEER}} \times A_{P,FEER} \tag{4}$$

258 where $\widehat{E}_{PM_{FEER}}$ is the area-normalized daily average E_{PM} from each FEER pixel, and $A_{P,FEER}$ is
259 the FEER grid cell area (0.1° x 0.1°). The summation is over all FEER grid cells per fire. FEER
260 grid cells are included if they are within 0.1° of the centroid of the final GeoMAC fire perimeter
261 for each fire. We convert from UTC time to local time following the same approach described in
262 section 2.1.1. We also calculate the average FEER C_e for the fires sampled during the western
263 portion of the FIREX-AQ campaign as the average of all C_e estimates in every 1° grid cell that
264 encompassed at least a fraction of the final GeoMAC perimeter of a fire.
265 We estimate relative uncertainty in FEER E_{PM} estimates by propagating uncertainty
266 through equation 3. We calculate the relative uncertainty of C_e as the standard deviation divided
267 by the mean of all extracted FEER C_e values used in this analysis, and we obtain the relative
268 uncertainty of MODIS FRP from Freeborn et al. (2014). FEER C_e for Western US wildland fires
269 has a relative uncertainty of 73% and FRP has a relative uncertainty of 27%, yielding a relative
270 uncertainty in FEER E_{PM} of 78% (Supplementary Table S1).

2.2 Emission Rate Estimates from FIREX-AQ

2.2.1 In Situ Measurement Approach (High-Resolution)

273 We capitalize on the intensive, high spatial and temporal resolution smoke plume
274 measurements from the DC-8 aircraft during FIREX-AQ to calculate E_C and E_{PM} via a novel in
275 situ measurement-driven approach. We assume fire emission rates over time are equal to the flux
276 of smoke as it passes through a vertical slice of the smoke plume, represented as an HSRL

277 curtain measured during in situ transects (Figure 1). We calculate E_C and E_{PM} for each wildland
278 fire sampled during FIREX-AQ on a sub-plume (per transect) basis as

$$E_X = \overline{WS} \times \overline{GS} \times \sum_{t_{start}}^{t_{end}} \Delta X_t \times H_t \Delta t \tag{5}$$

280 where E_x is the emission rate of species X (either carbon or PM), $\overline{WS}$ is the transect average wind
281 speed, $\overline{GS}$ is the transect average ground speed, ΔX_t is the excess concentration of species X
282 averaged over 10 second intervals to match the horizontal resolution of the HSRL data collected
283 at aircraft measurement time t, and H_t (m) is the plume thickness measured by the nadir and
284 zenith pointing HSRL profiles at aircraft measurement time t (Hair et al., 2008). This approach
285 assumes that the vertical distribution of each species is uniform, and the lidar is used to find the
286 vertical extent of the plume. Excess concentrations are calculated by subtracting a background
287 concentration defined as the average concentration 5-10 seconds prior to the start of the transect
288 and 5-10 seconds after the end of the transect. In a few cases, the PM background is elevated
289 during the time interval used to define a background such that the excess mixing ratio is
290 computed as a negative value, and these cases are excluded from the analysis. The time interval
291 from t_{start} to t_{end} is equal to the length of time to complete each transect, and Δt is ~10 seconds,
292 which is the horizontal resolution of the HSRL data. H_t is calculated as the sum of HSRL profile
293 bin heights (Δz_t) where the particle backscatter coefficient (β_t) is greater than 1 km^{-1} sr^{-1}, which
294 was larger than the average background scattering and defined the smoke plume edges for the
295 cases sampled.

$$H_t = \sum_{z=0}^{z=\infty} \Delta z_t [\beta_t > 1 \text{ km}^{-1} \text{ sr}^{-1}] \tag{6}$$

297 In exceptionally dense smoke plumes, the HSRL laser light was fully attenuated before it
298 could completely pass through the smoke plume edge, and for these cases we assume the smoke
299 plume extended to the surface and neglect the missing portion of the plume above the aircraft.
300 This approach is reasonable as the aircraft tended to sample the smoke plumes near the top of the
301 atmospheric boundary layer, which places a weak upper constraint on the top of the plume just as
302 the surface places a lower constraint on boundary layer mixing processes. An alternative
303 approach to calculate plume thickness using HSRL observations leverages the ratio of the
304 backscatter coefficient in a single HSRL bin to the sum of all backscatter coefficients in a
305 vertical column. We estimate the sensitivity of plume thickness to these two approaches and
306 discover strong agreement (slope = 0.72, r = 0.83), although the alternative approach estimates
307 slightly lower plume thickness on average (Figure S1). We ultimately choose the approach to
308 calculate plume thickness as outlined in equation 6 in an effort to avoid additional uncertainty
309 from relying more heavily on the backscatter coefficient, which may be confounded by changes
310 in aerosol size and/or optical properties rather than mass loading.
311 Total PM is calculated as the sum of organic aerosol (OA), sulfate, nitrate, ammonium,
312 and black carbon aerosol (BC) reported at standard temperature and pressure conditions and
313 converted to ambient volumetric units. The 50% geometric transmission diameter for the AMS is
314 approximately 600nm, which sufficiently captures the size range for the majority of biomass
315 burning derived particles, with the exception of supermicron ash particles (Adachi et al., 2021;
316 Moore et al., 2021). All components of the submicron non-refractory total PM concentrations are
317 measured using an Aerodyne Time of Flight Aerosol Mass Spectrometer (ToF-AMS)
318 (Canagaratna et al., 2007; DeCarlo et al., 2006; Guo et al., 2021) . Refractory BC mass
319 concentrations are provided by a Single Particle Soot Photometer (SP2, Droplet Measurement
320 Technologies). Total carbon is calculated as the sum of CO_2, CO, CH_4, organic carbonaceous

321   aerosol (OC), and BC aerosol. OC is estimated using the OA to OC ratio provided by the ToF-
322   AMS. The CO_2 mixing ratio measurements are obtained using a non-dispersive infrared (IR)
323   spectrometer (LICOR, Inc. Model 7000) adapted for aircraft measurements in a method similar
324   to Vay et al. (2003), while CO and CH_4 mixing ratios are obtained from mid-IR laser absorption
325   spectrometry (Sachse et al., 1991). All three trace gas species were calibrated in-flight with
326   standards from the National Oceanic and Atmospheric Administration Earth Science Research
327   Laboratories (NOAA ESRL) traceable to World Meteorological Organization (WMO) scales.
328   The trace gas measurements were converted from mole fractions to ambient volumetric units by
329   multiplying the mixing ratio by the ratio of the molecular weight to the molecular volume at
330   ambient temperature and pressure conditions.

331   We estimate relative uncertainty in E_C and E_{PM} using equations 5 and 6. We calculate the
332   following relative uncertainties: WS = 20%, GS = 3%, H_t = 28%, ΔC = 56%, and ΔPM = 67%.
333   The relative uncertainty for each variable is assumed to be equal to the mean divided by the
334   standard deviation of observations collected during all smoke plume transects. The computed
335   relative uncertainty in E_C is 66% and the relative uncertainty in E_{PM} is 75% (Supplementary
336   Table S1).

337   **2.2.2 Fuel2Fire (High-Resolution Bottom-up)**

338   E_C estimates for all FIREX-AQ wildland fires derived using a bottom-up style approach
339   are publicly available on the FIREX-AQ data archive
340   (https://doi.org/10.5067/SUBORBITAL/FIREXAQ2019/DATA001). This dataset, the Fuel2Fire
341   carbon emissions inventory, is optimized and designed to estimate carbon emissions specifically
342   for the fires sampled during FIREX-AQ. We use Fuel2Fire E_C estimates for the high-resolution
343   bottom-up approach to estimate E_C and E_{PM} on a per transect basis for each of the fires included
344   in this analysis. As a bottom-up inventory, Fuel2Fire calculates E_C in the same way as GFED,
345   following equation 1. The Fuel2Fire emissions inventory derives burned area using a
346   combination of active fire detections from MODIS, VIIRS, and/or Geostationary Operational
347   Environment Satellite Program (GOES-16 and 17 ABI L2 +). Active fire pixels from one or
348   more of these active fire detection products are selected to best match ground-verified
349   interagency situational reports from fire management teams, as well as GeoMAC fire perimeters.
350   Fuel2Fire determines fuel loading using ultra high-resolution (30 meter) fuels data from the
351   Fuels Characteristics and Classification System (FCCS) and models combustion completeness as
352   a function of daily fire weather danger ratings. Total daily carbon emissions are temporally
353   distributed using a diurnal cycle of fire activity derived from geostationary satellite observations
354   of FRP from GOES-16 and 17. Fuel2Fire assumes F_C is 0.5 kg kg^{-1} (McMeeking et al., 2009;
355   Santín et al., 2015; Yokelson et al., 1997). The archived carbon emissions data has a native
356   temporal resolution that matches GOES-16 and 17 data (5 minutes) and is linearly interpolated to
357   1 Hz data for consistency with the aircraft data. E_C estimates from Fuel2Fire extend over the
358   course of an entire 24-hour day (local time) that a given fire was sampled during FIREX-AQ.

359   We convert E_C estimates from the Fuel2Fire inventory to E_{PM} as follows

360
$$E_{PM} = \frac{E_C \times EF_{PM}}{F_C} \tag{7}$$

361   Here, we obtain E_C from the Fuel2Fire inventory, while EF_{PM} is calculated using aircraft
362   observations. We choose to calculate EF_{PM} from in situ observations as opposed to assuming
363   EF_{PM} from a compilation of previous studies in order to investigate the potential influence of the
364   choice in EF_{PM} on differences in emission rate estimates. F_C is assumed to be 0.5 kgC kg-fuel^{-1},

365   but we note F_C can vary from 0.35-0.55 (Akagi et al., 2011; Burling et al., 2010; McMeeking et
366   al. 2009; Susott, 1996). We calculate EF_{PM} for each in situ smoke plume transect using airborne
367   measurements following the carbon mass balance approach (Ward & Radke, 1993; Yokelson et
368   al., 1996, 1999). Although the smoke age and, thus, probability of plume processing increases as
369   a function of downwind distance from the fire, we assume PM is conserved over the relatively
370   short period of time (0.5-7 hrs) that the smoke has been exposed to atmospheric aging processes
371   when it was sampled by the DC-8 and attribute any changes in mass concentration to variability
372   in fire activity (Garofalo et a., 2019; Hodshire et al., 2019). The time of emission is not the same
373   as when the DC-8 sampled the plume, so we correct for this time offset by adding smoke age to
374   the time of emission when determining the Fuel2Fire total carbon emission rates on a sub-plume,
375   per transect basis. The smoke age is calculated for each point on the DC-8 transect assuming
376   horizontal straight line advection of the smoke plume at the DC-8 measured wind speed
377   (Wiggins et al., 2020).
378   We estimate relative uncertainty in E_C and E_{PM} derived from Fuel2Fire by propagating
379   uncertainty through equation 7. The relative uncertainty in E_C is assumed to be 55%, calculated
380   by taking the average divided by the standard deviation of all computed E_C estimates for each
381   fire and every transect included in this analysis. The relative uncertainty in EF_{PM} is 39%,
382   computed as the mean of all calculated EF_{PM} for all fires divided by the standard deviation. The
383   relative uncertainty in E_{PM} is thus 67% (Supplementary Table S1).

384   **2.2.3 HSRL-GOES (High-Resolution Top-down)**

385   We use FIREX-AQ aircraft-based HSRL measurements of aerosol extinction and
386   geostationary satellite observations of FRP from GOES to calculate E_{PM} using a high-resolution
387   top-down approach, referred to as HSRL-GOES. We use the same equation that is used in FEER
388   (Equation 3) to calculate E_{PM} for the western fires sampled during FIREX-AQ on a per transect
389   basis for the high-resolution top-down approach. Instead of using MODIS FRP, we obtain FRP
390   from the GOES-16 and GOES-17 ABI L2 + Fire/hot spot Detection and Characterization product
391   from the Wildfire Automated Biomass Burning Algorithm processing system (Schmidt, 2019).
392   GOES has an exceptionally high temporal resolution (~5-15 mins) with FRP observations that
393   cover the entire continental US at a spatial resolution of 2km (Schmidt, 2019). We time align
394   GOES FRP observations to match the in situ plume sampling time by adding the smoke age to
395   the FRP observation time, and we include all FRP observations within 4km (the spatial
396   resolution of GOES-16 and 17) of a given fire's final GeoMAC perimeter centroid. FRP per
397   transect is calculated as the sum of all instantaneous FRP observations for a given fire averaged
398   over the in situ plume sampling time for a given transect. The smoke emission coefficient is also
399   calculated for each fire on a per transect basis as follows:

400

401              $$C_e = \frac{\overline{WS \times GS}}{\overline{MEE} \times \overline{FRP_f}} \times \sum_{t_{start}}^{t_{end}} \Delta AOT_t \, \Delta t \qquad\qquad (8)$$

402

403   where $\overline{FRP_f}$ is the time-aligned, transect-average GOES FRP, $\overline{MEE}$ is the transect average MEE
404   calculated from in situ measurements as described below, and ΔAOT is aerosol optical thickness

405 derived from vertically integrating the background-subtracted 532nm HSRL particle extinction
406 coefficient ($\Delta\alpha$) as described by

407

408
$$\Delta AOT_t = \int \Delta\alpha_t \Delta z \tag{9}$$

409

410 HSRL is not able to collect measurements immediately above and below the aircraft. We linearly
411 interpolated through the 60m aircraft gap in the HSRL curtains to account for the missing data.
412 Background extinction is defined as the average HSRL extinction profile 10 sec before and after
413 the smoke plume transect. In cases where the laser light fully attenuated before it reached the
414 bottom of the plume, we assume the plume extended to the surface and extrapolate extinction to
415 the ground using the closest measurement to the surface. In limited cases where the beam is
416 completed attenuated in the zenith direction, we integrate over the measured range but do not add
417 any correction as this is expected to be a relatively small contribution as the aircraft was typically
418 flying near the top of the atmospheric boundary layer near plume top. We use the high-resolution
419 in situ measurements from the DC-8 to calculate MEE; however, we note that most top-down
420 inventories (such as FEER) assume a constant MEE of 4.6 $m^2\,g^{-1}$ derived from previous studies.
421 We calculate transect average MEE as the slope of an reduced major axis regression with a
422 forced zero intercept between total PM and the dry aerosol extinction coefficient at 532nm for
423 each transect. The extinction coefficient is calculated as the sum of dry scattering and absorption
424 coefficients measured by a TSI-3563 Nephelometer at 550nm and a 3-wavelength Particle Soot
425 Absorption Photometer at 532nm (PSAP, Radiance Research) respectively. Scattering
426 coefficients are converted to 532nm to match the absorption coefficients using the angstrom
427 exponent as calculated by the blue and green channels from the nephelometer. Scattering
428 coefficients are corrected for truncation errors following Anderson and Ogren (1998), and PSAP
429 absorption data are corrected following Virkkula et al. (2010). The aerosol extinction
430 humidification factor, f(RH) is assumed to be unity, which is consistent with the FIREX-AQ in-
431 plume measurements.
432   We estimate the uncertainty in HSRL-GOES E_{PM} by propagating uncertainty through
433 equation 3, where the relative uncertainty in C_e derived following equation 8 is calculated as the
434 mean C_e from all fires divided by the standard deviation (67%), and the relative uncertainty in
435 FRP is assumed to be 40% (Li et al., 2020). The relative uncertainty in HSRL-GOES E_{PM} is thus
436 77% (Supplementary Table S1).

437 **2.3 Comparison of Approaches**

438   We summarize the approaches and relevant equations used in this study to calculate E_C
439 and E_{PM} in Table 1. We evaluate emission rate estimates between the high-resolution bottom-up
440 (Fuel2Fire) and top-down (HSRL-GOES) based approaches against the in situ approach on a per
441 transect basis for individual wildland fires sampled during FIREX-AQ. The relationship between
442 the different approaches is quantified using the slope of a reduced major axis regression with a
443 forced zero intercept, a Pearson's correlation coefficient, and root mean square error (RMSE).
444 These calculations are performed as a campaign level summary that includes all transects and all
445 fires and for each fire individually.
446   We compare daily (24 hour local time) average E_{PM} estimates from the three high
447 resolution approaches (In Situ, Fuel2Fire, and HSRL-GOES) to daily average estimates derived

448 from lower resolution global fire emissions inventories (GFED and FEER). These comparisons
449 are performed on daily average emission rate estimates, as opposed to estimates on a per transect
450 basis, because of the lower temporal resolutions of GFED (3 hr/daily) and FEER (daily).

451 **2.4 Smoke Emission Coefficients**

452   The high spatial and temporal resolution of the in situ, bottom-up (Fuel2Fire), and top-
453 down (HSRL-GOES) based approaches provide the opportunity to evaluate smoke emission
454 coefficients that are usually derived using many years of data. Smoke emission coefficients for
455 PM are calculated as the slope of a reduced major axis regression with a forced zero intercept
456 between GOES FRP time aligned to the transect sampling time versus E_{PM} for each of the three
457 high resolution approaches. These computations are also executed as a campaign level summary
458 and for each fire individually. We compare our C_e from the high resolution approaches to the
459 average FEER C_e for the western fires sampled during FIREX-AQ.

460 **3 Results and Discussion**

461 **3.1 Total Carbon Emission Rates**

462   The derivation of the variables used to calculate E_C using bottom-up approaches are
463 based on assumptions that can lead to both under and overestimation, depending on the data
464 products leveraged by a given fire emissions inventory. We uncover a significant relationship
465 between E_C per transect derived from the high-resolution bottom-up approach (Fuel2Fire) and
466 the in situ approach as shown in Figure 2 (slope = 1.00, r = 0.82). However, there is also a non-
467 trivial level of scatter in this relationship (RMSE = 67%), and individual fires considered
468 separately have different correlations and regression slopes.
469   From Figure 3, we similarly find strong, linear correlations between daily fire average E_C
470 from the in situ measurement based estimates and Fuel2Fire (slope = 1.09, r = 0.92, RMSE =
471 61%) and GFED (slope = 0.20, r = 0.87, RMSE = 132%). The daily average E_C estimated using
472 Fuel2Fire are marginally higher than estimates derived from the in situ approach, while the
473 GFED estimates are 80% lower. The strong correlation, but significant offset between GFED and
474 the in situ measurement based approach implies that there may be a systematic bias in one or
475 more of the variables used to calculate the mass of biomass consumed in some traditional
476 bottom-up inventories. In this section, we examine the assumptions and uncertainty in individual
477 variables used to calculate E_C using a bottom-up approach in an effort to understand the
478 differences in E_C estimates derived from Fuel2Fire and GFED relative to the in situ approach.

479   **3.1.1 Carbon Mass Balance**

480   The key assumption in a bottom-up approach is that all burnt carbon is volatilized and
481 released into the atmosphere. This carbon mass balance assumption has recently been
482 scrutinized, because not all fuel that has been thermally altered by a fire is emitted to the
483 atmosphere (Santín et al., 2015; Surawski et al., 2016). Some of the burnt fuel remains on the
484 ground as charred biomass. If the carbon mass balance assumption does not hold, then this could
485 potentially cause an overestimation of carbon emissions derived from bottom-up approaches by
486 up to 50% in temperate forests, depending on levels of combustion completeness (Santín et al.,
487 2015). Our results do not show significant evidence of bias in E_C estimates from Fuel2Fire, but
488 do show a distinct low bias in estimates from GFED. This suggests there are underlying
489 confounding factors to disentangle before it is possible to determine if the assumptions inherent

490   in the carbon mass balance approach are responsible for a significant bias in bottom-up
491   inventories.

3.1.2 Burned Area

493   The two methods for calculating burned area using a bottom-up approach operate under
494   specific assumptions that could cause either an over or under estimation of carbon emissions.
495   The active fire based method has the potential to overestimate burned area, because it assumes
496   all the area within the resolution of a single active fire detection is burned. Conversely, the
497   burned area based method using MODIS burned area data products (MCD65A1) has been shown
498   to underestimate burned area, because of high omission error in grid cells with smaller
499   proportions of burned area (Boschetti et al., 2019). A recent validation study that compares 500-
500   meter resolution MODIS burned area products (MCD64A1) against 30-meter resolution Landsat
501   data found MODIS underestimated global burned area by 54% (Boschetti et al., 2019). However,
502   MODIS burned area products also have a non-trivial level of uncertainty, approximately 44%
503   (Giglio et al., 2018).
504   Fuel2Fire, calculates burned area using the active fire approach, while GFED uses
505   MODIS burned area data products. GFED4.1s attempts to address the known small fire driven
506   burned area underestimation from MODIS using a supplementary algorithm known as the small
507   fire boost (Randerson et al., 2012; van der Werf et al., 2017). We compare the GFED and
508   Fuel2Fire burned area estimates in Figure S2, which are in good agreement for the western fires
509   sampled during FIREX-AQ (slope = 0.97, r = 0.93). This indicates that the differences in the two
510   approaches to calculate burned area are not responsible for the low bias we see in GFED
511   emission rate estimates.

3.1.3 Combustion Completeness

513   All state-of-the-art approaches to calculate combustion completeness rely on daily or
514   monthly average observations, and therefore cannot accurately estimate the pronounced sub-
515   daily changes in combustion completeness that occur throughout the diurnal cycle of fire
516   activity. Instead, these methods assume combustion completeness can be estimated using
517   observations averaged over large areas. Combustion completeness in the Fuel2Fire inventory is
518   based on daily fire weather indices, where higher levels of fire danger equate to higher
519   consumption rates, while GFED relies on a biogeochemical model with a monthly time step to
520   estimate combustion completeness.
521   We expect GFED combustion completeness to be overestimated on days with low fire
522   activity and underestimated on days with high fire activity as a result of the monthly averaging
523   scheme, however that is not the observed trend (Figure 3). Instead, GFED underestimates E_C for
524   almost every fire included in this analysis. It is therefore unlikely that differences in the
525   approaches to calculate combustion completeness strongly contribute to the systematic low bias
526   found in GFED E_C estimates.

3.1.4 Fuel Loading

528   The complexity and variability of fuel type (or land cover) and loading are difficult to
529   accurately represent and validate. Labor intensive high spatial resolution fuel databases, such as
530   the FCCS database used in the Fuel2Fire inventory, are derived from a compilation of previous
531   remote sensing studies, government databases, photos, in situ measurements, and expert opinion
532   (Ottmar et al., 2007). The spatial resolution of FCCS is 30m; however, this resolution is achieved

533   through the extrapolation of field-based measurements to ecosystem scales, which relies on a
534   number of strong assumptions that infer the distribution and composition of fuels from the same,
535   similarly-aged, spectrally-similar ecosystems are roughly spatially constant. Fuels are constantly
536   changing in response to seasonal, environmental, and anthropogenic forcing, but the laborious
537   effort required to develop fuel databases severely restricts the rate at which they can be updated.
538   As a result, fuel bed databases can remain unchanged and out of date for a number of years
539   before updates are implemented. This delay can exacerbate the uncertainty and error in fuel
540   loading estimates. Model based estimates of fuel loading that rely on remote sensing
541   observations of surface characteristics, like those used in GFED, are similarly challenged by the
542   limited number of field measurements available to validate estimates. Potential bias stemming
543   from fuel loading estimates can be negative or positive, depending on the accuracy of initial
544   estimates and if the database or model correctly implements changes in fuel loading following
545   ecosystem disturbance mechanisms including fire.
546   We discover an exceptional uncertainty in GFED fuel loading (111%), however the
547   uncertainty in the FCCS fuels database used by Fuel2Fire is estimated to be much lower (~70%)
548   (Keane et al., 2013) (Supplementary Table S1). Combined with the lack of evidence that burned
549   area or combustion completeness significantly contribute to GFED emission estimate bias, this
550   implies the differences in fuel loading estimates from the model used in GFED versus the high-
551   resolution fuels database (FCCS) used in Fuel2Fire is the most likely culprit for the persistent
552   underestimation of GFED E_C estimates from Western US wildland fires. The agreement we see
553   in E_C estimates from Fuel2Fire versus the in situ based approach provides confidence for the use
554   of high resolution fuels databases such as FCCS (Figure 2).
555   Previous studies aimed at quantifying uncertainty in the parameters used by bottom-up
556   inventories to calculate emissions have also identified fuel loading as a major source of
557   uncertainty (French et al., 2004; Urbanski et al., 2011; Prichard et al., 2019). Furthermore, fuel
558   loading uncertainty likely fluctuates considerably as a function of vegetation type, due to scarce
559   field validation studies for certain ecosystems and/or mapping errors. Our results highlight the
560   need for additional field validation studies to constrain fuel loading estimates.

561   **3.2 Total PM Emission Rates**

562   We find the strong relationship between Fuel2Fire and the in situ based method persists
563   for E_{PM} at a sub-plume scale, albeit with a similarly high level of scatter as shown in Figure 4a
564   (slope = 0.90, r = 0.77, RMSE = 61%). We derive EF_{PM} from the in situ FIREX-AQ
565   measurements on a per transect basis in order to minimize the potential influence of emission
566   factor uncertainty in Fuel2Fire E_{PM} estimates. The high level of spread in the data is likely an
567   artifact of the uncertainty in E_C from Fuel2Fire caused by the biases and sources of uncertainty
568   discussed in Section 3.1, most notably the impacts of fuel loading uncertainties. Additionally,
569   this comparison is based on the assumption that the transport of fire emissions from the ground
570   to the in-situ transect is accurately modeled in both space and time.
571   Figure 4b shows a significant relationship between E_{PM} calculated using HSRL-GOES
572   and the in situ approach at a sub-plume scale (slope = 1.04, r = 0.82, RMSE = 48%). While there
573   is a marginally lower level of scatter in this relationship as shown by the RMSE, HSRL-GOES
574   slightly overestimates E_{PM} on the lower end of the scale compared to the in situ approach. This
575   overestimate implies from Equation 3 that either or both the GOES FRP and C_e for these fire
576   transects are biased high, where it follows from Equation 12 that the latter may be influenced by
577   a low estimate of the smoke MEE or a high estimate of the optical thickness. A high optical

578 thickness bias might be due to the extrapolation of HSRL extinction to the surface for cases
579 when the laser light fully attenuates; although, we note the bias is most significant for the lower
580 emission rates, which might discount this hypothesis.
581   We find strong correlations between daily average E_{PM} estimates from the in situ
582 approach versus estimates from both of the high-resolution approaches, Fuel2Fire (slope = 1.04,
583 r = 0.93, RMSE = 39%) and HSRL-GOES (slope = 1.18, r = 0.89, RMSE = 47%) (Figure 5). The
584 correlation is weaker and the spread is larger between the in situ based estimates and estimates
585 from the lower-resolution global inventories, GFED and FEER. The systematic low bias seen in
586 GFED daily average E_C estimates is also seen for daily average E_{PM} for all but the smallest fires
587 (slope = 0.21, r = 0.85, RMSE = 104%). FEER slightly underestimates E_{PM} from larger fires that
588 emit relatively more PM and overestimates E_{PM} from smaller fires that emit relatively less PM
589 (slope = 1.38, r = 0.64, RMSE = 55%). FEER provides no E_{PM} estimates for the Castle fire on
590 both days of sampling, and we exclude these zero estimates from this fire when computing the
591 linear regression and correlation coefficient given their disproportionate weight in skewing the
592 regression.
593   Global fire emissions inventories are known to significantly differ on E_{PM} estimates from
594 temperate fires, especially in North America (Nikonovas et al., 2017; Pan et al., 2020). In the
595 following sections we use the high resolution airborne in situ measurements of smoke plumes
596 collected during FIREX-AQ to isolate the assumptions and variables responsible for the
597 discrepancy and quantify their relative contributions.

598   ### 3.2.1 Emission Factors

599   Emission factors are used in bottom-up approaches to convert carbon emissions to
600 emissions of a specific trace gas or particulate species, and emission factor estimates usually
601 come from compilation studies that include in situ measurements from wildland fires and
602 laboratory experiments (Akagi et al., 2011; Andreae, 2019; Andreae & Merlet, 2001; May et al.,
603 2014). The use of such emission factors relies on the assumption that the most representative
604 value can be approximated as the mean of all previous studies. In reality, emission factors are
605 dynamic and vary as a function of combustion completeness, which can fluctuate both spatially
606 and temporally for a given fire. Laboratory studies struggle to represent the complexity of a
607 wildland fire and can disagree with in situ measurements, while in situ measurements are subject
608 to sampling bias (Hodshire et al., 2019; Yokelson et al., 2013). For example, airborne based
609 measurements tend to be limited to daytime sampling of well-developed plumes that have risen
610 to an altitude that is accessible by the aircraft. Consequently, these measurements may be biased
611 towards flaming combustion because nighttime and/or smoldering emissions resulting from less
612 energetic fire activity are not being sampled (Burling et al., 2011; Prichard et al., 2020; Wiggins
613 et al., 2021). The suggested EF_{PM} for temperate forests from GFED is 17.6 g kg^{-1}, and the mean
614 EF_{PM} we calculated using FIREX-AQ in situ airborne measurements is 15.8 ± 4.3 g kg^{-1}, which
615 is well within range of the suggested EF_{PM} from GFED. Our results suggest EF_{PM} does not
616 strongly contribute to bias in bottom-up emission rate estimates from Fuel2Fire or GFED for the
617 fires sampled during FIREX-AQ. However, we acknowledge this analysis focused exclusively
618 on fires with well-developed plumes that were sampled during the daytime, and thus may not be

619 subject to EF_{PM} discrepancies that can occur as a result of under sampled smoldering
620 combustion.

3.2.2 Smoke Emission Coefficient (C_e)

622 Smoke emission coefficients used by top-down inventories to convert FRP to E_{PM} are
623 typically derived using multiple years of AOD and FRP observations, but here we use high
624 resolution measurements from FIREX-AQ to calculate C_e over a limited duration for a small
625 number of fires. We find strong to moderate linear relationships between GOES FRP
626 observations and the calculated emission rates from the high resolution in situ approach (C_e = 5.0
627 gPM MW^{-1}, r = 0.75, RMSE = 165%), Fuel2Fire (C_e = 8.2 gPM MW^{-1}, r = 0.94, RMSE = 46%),
628 and HSRL-GOES (C_e = 8.4 gPM MW^{-1}, r = 0.72, RMSE = 75%) (Figure 6). Individual fires
629 have significantly different C_e, and vary depending on which approach was used to calculate E_{PM}
630 (Table 3), which highlights the sensitivity and natural variability of this parameter. All three of
631 the high resolution approaches estimate a lower C_e for the set of Western US wildland fires
632 included in this study compared to the estimated C_e from FEER (10.6 gPM MW^{-1}). However, the
633 calculated C_e are within the large uncertainty (50%) of the C_e for western US fires derived from
634 FEER, and the RMSE is substantial for the in situ approach and HSRL-GOES.
635 Fuel2Fire temporally distributes emissions using the diurnal cycle of GOES FRP
636 observations, which explains the exceptionally strong linearity and correlation between GOES
637 FRP and E_{PM} estimates in Figure 6b. HSRL-GOES E_{PM} estimates shown in Figure 6c continue to
638 have a slight high bias on the lower end of the scale. We find a high bias in E_{PM} for the Castle
639 fire in all three high resolution approaches compared to what would be expected based on the
640 overall campaign level relationship between FRP and emission rates (Figure 6). The Castle fire
641 had the lowest average excess PM concentrations per transect out of all the fires included in this
642 analysis. The elevated emission rates from all three approaches indicate GOES likely missed
643 some of the FRP, likely due to low temperature smoldering or cloud cover, which is consistent
644 with the low fire severity measured in post-burn satellite data.
645 FEER uses MODIS FRP observations to calculate C_e, but we use GOES FRP. There
646 could be a potential offset between FRP observations between MODIS and GOES as a result of
647 differences in instrument resolution and saturation levels as well as overpass time effects (Li et
648 al., 2019; Xu et al., 2021). The coarse spatial resolution of GOES (2km) limits its capability to
649 detect cool or small fires with low FRP, and could result in an underestimation of FRP by up to
650 50% globally (Freeborn et al., 2008), which would explain the difference in C_e estimated using
651 the high resolution approaches versus FEER. We use GOES FRP because of the exceptionally
652 high time resolution (5-15 mins) over the continental US versus the twice daily temporal
653 resolution of MODIS or VIIRS. This allows for a more direct comparison between in situ
654 measurements and remote sensing observations.
655 Previous studies have suggested E_{PM} and thus C_e calculated using MODIS AOD may be
656 systematically biased low, because of a discrepancy between observed AOD from MODIS
657 versus AERONET and MISR (Pan et al., 2020). However, we find agreement between E_{PM}
658 calculated independently of MODIS AOD and E_{PM} estimated from FEER, which relies on
659 MODIS AOD observations. The results suggest MODIS AOD observations can be used to

660 accurately represent atmospheric aerosol mass loading of particulates emitted by Western US
661 wildland fires.

3.2.2.1 Mass Extinction Efficiency (MEE)

663   The conversion of FRP to PM assumes that variability in particle extinction, and thus
664 AOD, is driven by changes in aerosol mass concentration rather than aerosol intensive
665 properties. Estimates of particle mass extinction efficiency (MEE) are essential to the conversion
666 of AOD to total PM. However, aerosol extinction and other optical properties depend on particle
667 size, morphology, and chemical composition (Seinfeld & Pandis, 2006). The characteristics of
668 biomass burning aerosols are known to vary with fuel type and combustion completeness
669 (McClure et al., 2020; Reid et al., 2005a; Reid et al., 2005b). Furthermore, the physical and
670 optical properties of smoke aerosols rapidly evolve following emission as a result of
671 photochemical aging and aerosol microphysical processes (Akagi et al., 2012; Cappa et al., 2020;
672 Garofalo et al., 2019; Hodshire et al., 2019; May et al., 2014; Shingler et al., 2016). Particle
673 evolution via these processes is additionally influenced by external factors, such as the fire size,
674 rate of dilution, and background aerosol concentrations (Hodshire et al., 2019). The assumption
675 that variability in AOD is entirely due to changes in particle concentration oversimplifies the
676 complex interactions of smoke particle microphysical processes and photochemical aging. Some
677 top-down inventories attempt to reconcile this discrepancy by calculating a separate C_e for each
678 individual ecosystem. However, this is likely not sufficient to fully address the variability in
679 smoke aerosol extinction that often occurs even in smoke plumes from fires within a single
680 ecosystem type.
681   Top-down inventories, including FEER, usually assume a constant MEE of 4.6 m^2 g^{-1}
682 based on a compilation of previous studies (Ichoku & Kaufman, 2005; Reid et al., 2005b). The
683 compilation found MEE varied between 3.4 – 5.1 m^2 g^{-1} for biomass burning particles of all ages
684 across a diverse set of ecosystems (Figure S3) (Reid et al., 2005b). We find MEE values vary
685 between 2 - 6 m^2 g^{-1} for the FIREX-AQ smoke plumes and that the MEE increases
686 asymptotically as a function of smoke age (Figure 7). Our observations indicate MEE approaches
687 the mean from previous studies as the smoke rapidly evolves in the early hours after emission.
688 The rate at which MEE increases with smoke age is variable among the fires included in this
689 analysis and does not appear to depend on the plume PM concentration. Our range of MEEs for
690 smoke plumes from Western US wildland fires using high-resolution in situ measurements is
691 larger than what has been observed in previous studies. Our results emphasize the variability that
692 can occur in smoke MEE, and suggest that the top-down approach is likely more sensitive to
693 MEE than previous studies imply. The use of a constant MEE could lead to a high bias for fires
694 with lower excess PM concentrations and a low bias for fires with higher excess PM
695 concentrations, which would explain the trend we see in Figure 5 where FEER underestimates
696 fire E_{PM} from the most actively burning fires and overestimates E_{PM} from smaller, weaker fires.

3.2.2.2 Instantaneous Observations of FRP and AOD

698   FEER uses daytime MODIS FRP and AOD observations to derive C_e and assumes that
699 the FRP at the time of observation is directly related to the smoke plume AOD. However, fires
700 have a clear, ecosystem dependent diurnal cycle with the time of peak fire activity depending on
701 the specific landcover, geographic location, elevation, slope, aspect, and type of fire (e.g.,
702 wildland, prescribed, crown, surface). FRP observations represent the instantaneous fuel
703 consumption and corresponding emissions of a given fire, but AOD observations represent the

704   total mass of aerosols emitted by a fire, including the time period when the fire was active before
705   the satellite overpass time. The variability in FRP that occurs over the course of a day has a clear
706   impact on the total mass of smoke particles in the plume as a function of downwind distance
707   from the fire and wind speed, but polar orbiters, like MODIS do not have the temporal resolution
708   to quantify this relationship. As a result, C_e derived using FRP and AOD observed after the peak
709   in diurnal fire activity are likely overestimated, while C_e derived using FRP and AOD observed
710   prior to the peak may be slightly underestimated. The exact nature and magnitude of the potential
711   bias would depend on a specific fire's diurnal cycle and the age of the smoke captured in the
712   satellite observations of AOD. With respect to the calculation of E_{PM} using a predetermined C_e,
713   the time offset between MODIS overpass times and peak diurnal fire activity could similarly
714   cause a bias. E_{PM} could potentially be biased high or low if the satellite overpass time occurred
715   either before or after the peak in diurnal fire activity, and if the observed FRP was higher or
716   lower than the daily average FRP.
717   A recent study by Mota and Wooster (2018) demonstrated fire emission rates can be
718   calculated at a high temporal and spatial resolution (hourly and 0.05° x 0.05°, respectively) using
719   a top-down approach that relies on geostationary satellite observations of FRP from the Spinning
720   Enhanced Visible and InfraRed Imager (SEVIRI) to avoid bias caused by inadequate sampling of
721   a fire's diurnal cycle. We compare geostationary satellite observations of FRP from GOES that
722   match the overpass times of MODIS with the average of all FRP observations over the course of
723   a day for each fire to investigate potential bias in E_{PM} estimates from FEER. The Western US
724   wildland fires sampled during FIREX-AQ exhibited peak fire activity from 3-6 pm local time
725   (Pacific daylight time, UTC-7) (Wiggins et al., 2020). Meanwhile, local MODIS overpass times
726   are ~10:30am for the Terra satellite and ~1:20pm for Aqua. We find average GOES FRP at the
727   time of the MODIS overpasses is double the daily average FRP from GOES (Figure S4), which
728   could be partially responsible for the overestimation in FEER E_{PM} estimates for smaller fires that
729   we see in Figure 5.

4 Summary and Conclusions

731   We present a comprehensive evaluation of total carbon and aerosol emission rate
732   estimates computed using the methodologies and assumptions that are commonly employed by
733   global inventories used by models. These emissions inventories have the monumental task of
734   capturing the composition, magnitude, and temporal variability of fire emissions from nearly
735   every ecosystem on Earth. They are critical for the representation of wildland fires in large scale
736   models, and only recently have sufficiently comprehensive observational datasets become
737   available to evaluate their performance. One such study is the joint NASA/NOAA FIREX-AQ
738   airborne mission that took place in 2019. Here, we extend the methods and assumptions
739   employed by emissions inventories to develop state-of-the-art, high-resolution emission rate
740   estimates for each of the western FIREX-AQ fires, which are based on detailed information
741   garnered from ground, airborne, and satellite assets.
742   We discover excellent agreement between the high-resolution emission rate estimates
743   calculated using integrated airborne in situ and lidar observations and the high-resolution top-
744   down (HSRL-GOES) and bottom-up (Fuel2Fire) estimates at unusually high sub-plume
745   spatiotemporal resolution. While there is considerable scatter in the one-to-one plots comparing
746   Fuel2Fire to the airborne in situ data, the emissions rate estimates for both total carbon and PM
747   are not consistently biased between these methodological approaches. HSRL-GOES appears to
748   slightly overestimate E_{PM} toward the lower end of the observed range of variability (which

749 appears to also scale with FRP). Emission rate estimates calculated using the lower resolution
750 global fire emissions inventories, FEER and GFED, have a weaker relationship with the high-
751 resolution approaches and show evidence of systematic bias, which is most apparent for GFED.
752   We discuss, in detail, the key assumptions employed by bottom-up approaches and
753 conclude that the strong performance of the Fuel2Fire inventory stems from detailed information
754 about fuel type and loading that are parameterized with significant uncertainty in the global
755 inventories. In addition, we note that the high-temporal resolution of the Fuel2Fire dataset also
756 allows it to capture the entire diurnal cycle of the fire activity, which also serves to improve its
757 predictive skill. This hints that the high temporal resolution of geostationary satellite
758 observations of FRP could be used to correct the bias caused by satellite overpass times. With
759 respect to top-down approaches, we find a larger range in MEE for this small subset of Western
760 US fires than what has been reported in a compilation of previous studies that includes MEE
761 from fires in a diverse selection of global ecosystems. The high resolution top-down approach
762 (HSRL-GOES) allowed for the application of variable MEE obtained from sub-plume in situ
763 measurements. HSRL extinction measurements of the smoke plumes sampled during FIREX-AQ
764 combined with geostationary satellite observations of FRP offered an exceptionally detailed
765 measure of AOD and FRP associated with the smoke plume. The use of a constant MEE to
766 convert AOD to PM in top-down approaches combined with bias from assumptions related to
767 instantaneous observations of FRP and AOD are likely responsible for the underestimation in
768 FEER E_{PM} for larger fires and overestimation for smaller fires.
769   Finally, it's important to note that it is not yet computationally practical or feasible for
770 global fire emissions inventories to achieve the level of complexity and detail in the high-
771 resolution approaches presented here. We use these approaches to investigate discrepancies
772 between top-down and bottom-up E_{PM} estimates for Western US wildland fires. However, this
773 collection of fires represents only a small subset of the total number of fires that burn every year
774 in the Western US and may not be a perfect representation of the complexity that can exist in fire
775 emissions. In short, we have the luxury of evaluating the skill of the global emissions inventories
776 for a small subset of wildland fires for which we have unprecedentedly comprehensive data, but
777 we would be wise to remember that the goal of global emissions inventories is to represent all
778 fires reasonably well rather than to represent a few fires perfectly. Consequently, it may be
779 premature to adopt new values for, e.g., the smoke emission coefficient based solely on the
780 FIREX-AQ dataset. Our analysis does emphasize areas of large uncertainty, however, that may
781 be improved. One is the estimate of fuel type and loading that likely contributes to the scatter we
782 see in the bottom-up emission rate estimates from GFED and Fuel2Fire. Burned area and aerosol
783 mass emission factors do not appear to be large sources of uncertainty as there is good agreement
784 seen for both GFED and Fuel2Fire for both of these metrics. The importance of the high-
785 temporal resolution observations of both FRP and smoke AOD afforded by the geostationary
786 satellites currently in orbit cannot be overstated, as a lack of complete orbital coverage is also
787 likely to be a strong contributor to the inventory emissions underestimates. The use of a constant
788 MEE to convert AOD to PM should be revisited in light of the much higher variability we find in
789 MEE observations for such a limited number of fires, which accentuates the need for additional
790 measurements of this key variable. In summary, both top-down and bottom-up global fire
791 emissions inventories suffer from assumptions that may hold true in the aggregate, but break
792 down on an individual fire basis. The strong agreement that we show here between the high-
793 resolution approaches holds promise for future fire emissions inventories as advances in remote

794 sensing, improved computational efficiency, and a more complete understanding of fire behavior
795 begin to offer opportunities to increase the accuracy and resolution of global fire inventories.

796 **Appendix: List of Variables and Common Units**

797 *Note: units are included here only as examples and do not consider any unit conversions that*
798 *may be necessary for the equations given in the text.*

799 α_t	HSRL extinction coefficient	km^{-1}
800 $A_{P,FEER}$	FEER pixel area	km^2
801 $A_{P,GFED}$	GFED pixel area	km^2
802 AOD	Aerosol optical depth	unitless
803 β	HSRL backscatter ratio	$km^{-1}\ sr^{-1}$
804 BA	Burned area	m^2
805 CC	Combustion completeness	%
806 C_e	Smoke emission coefficient	$gPM\ MW^{-1}$
807 ΔC	Excess mass concentration of C	$\mu gC\ m^{-3}$
808 ΔPM	Excess mass concentration of PM	$\mu gPM\ m^{-3}$
809 Δt	HSRL curtain pixel width	s
810 Δz	HSRL curtain pixel height	m
811 E_C	Emission rate of total carbon	$kgC\ s^{-1}$
812 $\hat{E}_C$	Area-normalized emission rate of total carbon	$kgC\ m^{-2}\ s^{-1}$
813 E_{PM}	Emission rate of total PM	$kgPM\ s^{-1}$
814 $\hat{E}_{PM}$	Area-normalized emission rate of total PM	$kgPM\ m^{-2}\ s^{-1}$
815 EF_{PM}	Particle mass emissions factor	$gPM\ kg\ biomass\ consumed^{-1}$
816 F_C	Mass fraction of carbon in the fuel	$gC\ kg\ biomass\ consumed^{-1}$
817 FL	Fuel loading	$g\ biomass\ m^{-2}$
818 FRP	Fire radiative power	MW
819 H	Plume vertical thickness	m
820 MEE	Particle mass extinction efficiency	$m^2\ g^{-1}$
821 $\overline{MEE}$	Aircraft transect-average MEE	$m^2\ g^{-1}$
822 PM	Particle mass concentration	$\mu gPM\ m^{-3}$
823 $\overline{GS}$	Transect-average DC-8 aircraft ground speed	$m\ s^{-1}$
824 $\overline{WS}$	Aircraft transect-average wind speed	$m\ s^{-1}$

835 **Conflict of Interest**

836   The authors declare no conflicts of interest or competing interests.

837   **Author Contributions**

842   **References**

843   Abatzoglou, J. T., & Williams, A. P. (2016). Impact of anthropogenic climate change on wildfire
844   across western US forests. *Proceedings of the National Academy of Sciences of the United*
845   *States of America*, *113*(42), 11770–11775. https://doi.org/10.1073/pnas.1607171113

846   Adachi, K., J. E. Dibb, E. Scheuer, J. M. Katich, J. P. Schwarz, A. E. Perring, B. Mediavilla, H.
847   Guo, P. Campuzano-Jost, J. L. Jimenez, J. Crawford, N. Oshima, M. Kajino, T. Kinase, L.
848   Kleinman, A. J. Sedlacek III, R. J. Yokelson, & P. R. Buseck (2021), Fine ash particles as a
849   major aerosol component in biomass burning smoke, submitted to *Journal of Geophysical*
850   *Research: Atmospheres.*

851   Akagi, S. K., Yokelson, R. J., Wiedinmyer, C., Alvarado, M. J., Reid, J. S., Karl, T., Crounse, J.
852   D. & Wennberg, P. O. (2011). Emission factors for open and domestic biomass burning for
853   use in atmospheric models. *Atmospheric Chemistry and Physics*, *11*(9), 4039–4072.
854   https://doi.org/10.5194/acp-11-4039-2011

855   Akagi, S. K., Craven, J. S., Taylor, J. W., McMeeking, G. R., Yokelson, R. J., Burling, I. R.,
856   Urbanski, S. P., Wold, C. E., Seinfeld, J. H., Coe, H. & Alvarado, M.J. (2012). Evolution of
857   trace gases and particles emitted by a chaparral fire in California. *Atmospheric Chemistry*
858   *and Physics*, *12*(3), 1397–1421. https://doi.org/10.5194/acp-12-1397-2012

859   Anderson, T. L. & Ogren, J. A. (1998). Determining aerosol radiative properties using the TSI
860   3563 integrating nephelometer. *Aerosol Science and Technology*, *29*(1), 57-69.
861   https://doi.org/10.1080/02786829808965551

862   Andreae, M. O. (2019). Emission of trace gases and aerosols from biomass burning – an updated
863   assessment, *Atmospheric Chemistry and Physics*, *19*(13), 8523–8546.
864   https://doi.org/10.5194/acp-19-8523-2019, 2019

865   Andreae, M. O., & Merlet, P. (2001). Emission of trace gases and aerosols from biomass
866   burning. *Global Biogeochemical Cycles*, *15*(4), 955–966.
867   https://doi.org/10.1029/2000GB001382

868   Boschetti, L., Roy, D. P., Giglio, L., Huang, H., Zubkova, M., & Humber, M. L. (2019). Global
869   validation of the collection 6 MODIS burned area product. *Remote Sensing of Environment*,
870   *235*, 111490. https://doi.org/10.1016/j.rse.2019.111490

871   Burling, I. R., Yokelson, R. J., Akagi, S. K., Urbanski, S. P., Wold, C. E., Griffith, D. W.,
872   Johnson, T. J., Reardon, J. & Weise, D. R. (2011). Airborne and ground-based

873 measurements of the trace gases and particles emitted by prescribed fires in the United
874 States. *Atmospheric Chemistry and Physics*, *11*(23), 12197-12216.
875 https://doi.org/10.5194/acp-11-12197-2011

876 Burling, I. R., Yokelson, R. J., Griffith, D. W., Johnson, T. J., Veres, P., Roberts, J. M.,
877 Warneke, C., Urbanski, S. P., Reardon, J., Weise, D. R. & Hao, W. M. (2010). Laboratory
878 measurements of trace gas emissions from biomass burning of fuel types from the
879 southeastern and southwestern United States. *Atmospheric Chemistry and Physics, 10*(22),
880 11115-11130. https://doi.org/10.5194/acp-10-11115-2010

881 Canagaratna, M. R., Jayne, J. T., Jimenez, J. L., Allan, J. D., Alfarra, M. R., Zhang, Q., Onasch,
882 T. B., Drewnick, F., Coe, H., Middlebrook, A. & Delia, A. (2007). Chemical and
883 microphysical characterization of ambient aerosols with the aerodyne aerosol mass
884 spectrometer. *Mass Spectrometry Reviews*, *26*(2), 85-222.
885 https://doi.org/10.1002/mas.20115

886 Cappa, C. D., Lim, C. Y., Hagan, D. H., Coggon, M., Koss, A., Sekimoto, K., Gouw, J. D.,
887 Onasch, T. B., Warneke, C. & Kroll, J. H. (2020). Biomass-burning-derived particles from a
888 wide variety of fuels-Part 2: Effects of photochemical aging on particle optical and
889 chemical properties. *Atmospheric Chemistry and Physics*, *20*(14), 8511–8532.
890 https://doi.org/10.5194/acp-20-8511-2020

891 Carter, T. S., Heald, C. L., Jimenez, J. L., Campuzano-Jost, P., Kondo, Y., Moteki, N., Schwarz,
892 J. P., Wiedinmyer, C., Darmenov, A. S., Silva, A. M. D. & Kaiser, J. W. (2020). How
893 emissions uncertainty influences the distribution and radiative impacts of smoke from fires
894 in North America. *Atmospheric Chemistry and Physics*, *20*(4), 2073–2097.
895 https://doi.org/10.5194/acp-20-2073-2020

896 Darmenov, A. S., & da Silva, A. (2013). *The Quick Fire Emissions Dataset (QFED) -*
897 *Documentation of versions 2.1, 2.2, and 2.4, NASA Technical Report Series on Global*
898 *Modeling and Data Assimilation, Volume 32*.

899 DeCarlo, P. F., Kimmel, J. R., Trimborn, A., Northway, M. J., Jayne, J. T., Aiken, A. C., Gonin,
900 M., Fuhrer, K., Horvath, T., Docherty, K. S. & Worsnop, D. R. (2006). Field-deployable,
901 high-resolution, time-of-flight aerosol mass spectrometer. *Analytical Chemistry*, *78*(24),
902 8281-8289. https://doi.org/10.1021/ac061249n

903 Dennison, P. E., Brewer, S. C., Arnold, J. D., & Moritz, M. A. (2014). Large wildfire trends in
904 the western United States, 1984-2011. *Geophysical Research Letters*, *41*(8), 2928–2933.
905 https://doi.org/10.1002/2014GL059576

906 Freeborn, P. H., Wooster, M. J., Hao, W. M., Ryan, C. A., Nordgren, B. L., Baker, S. P., &
907 Ichoku, C. (2008). Relationships between energy release, fuel mass loss, and trace gas an
908 aerosol emissions during laboratory biomass fires. *Journal of Geophysical Research:*
909 *Atmospheres*, *113*, D01301. https://doi.org/10.1029/2007JD008679

910 Freeborn, P. H., Wooster, M. J., Roy, D. P. & Cochrane, M. A. (2014). Quantification of MODIS
911 fire radiative power (FRP) measurement uncertainty for use in satellite-based active fire

912   characterization and biomass burning estimation. *Geophysical Research Letters*, *41*(6),
913   1988-1994. https://doi.org/10.1002/2013GL059086

914   French, N. H. F., Goovaerts, P., & Kasischke, E. S. (2004). Uncertainty in estimating carbon
915   emissions from boreal forest fires. *Journal of Geophysical Research: Atmospheres*, *109*(14),
916   14–22. https://doi.org/10.1029/2003JD003635

917   Fusco, E. J., Abatzoglou, J. T., Balch, J. K., Finn, J. T., & Bradley, B. A. (2016). Quantifying the
918   human influence on fire ignition across the western USA. *Ecological Applications*, *26*(8),
919   2388–2399. https://doi.org/10.1002/eap.1395

920   Garofalo, L. A., Pothier, M. A., Levin, E. J. T., Campos, T., Kreidenweis, S. M., & Farmer, D.
921   K. (2019). Emission and Evolution of Submicron Organic Aerosol in Smoke from Wildfires
922   in the Western United States. *ACS Earth and Space Chemistry*, *3*(7), 1237–1247.
923   https://doi.org/10.1021/acsearthspacechem.9b00125

924   Giglio, L., Csiszar, I., & Justice, C. O. (2006). Global distribution and seasonality of active fires
925   as observed with the Terra and Aqua Moderate Resolution Imaging Spectroradiometer
926   (MODIS) sensors. *Journal of Geophysical Research: Biogeosciences*, *111*(2), 2016.
927   https://doi.org/10.1029/2005JG000142

928   Giglio, L., Boschetti, L., Roy, D. P., Humber, M. L. & Justice, C. O. (2018). The Collection 6
929   MODIS burned area mapping algorithm and product. *Remote Sensing of Environment*, *217*,
930   72-85. https://doi.org/10.1016/j.rse.2018.08.005

931   Goldammer, J. G., Statheropoulos, M., & Andreae, M. O. (2008). Impacts of Vegetation Fire
932   Emissions on the Environment, Human Health, and Security: A Global Perspective.
933   *Developments in Environmental Science*, *8*, 3-36. https://doi.org/10.1016/S1474-
934   8177(08)00001-6

935   Guo, X., Shang, Y., Lv, Y., Bai, H. & Ma, Q. (2021). Suspect Screening of Fentanyl Analogs
936   Using Matrix-Assisted Ionization and a Miniature Mass Spectrometer with a Custom
937   Expandable Mass Spectral Library. *Analytical Chemistry*, *93*(29), 10152-10159.
938   https://doi.org/10.1021/acs.analchem.1c01117

939   Harvey, B. J. (2016). Human-caused climate change is now a key driver of forest fire activity in
940   the western United States. *Proceedings of the National Academy of Sciences of the United
941   States of America*, *113*(42), 11649-11650. https://doi.org/10.1073/pnas.1612926113

942   Hodshire, A. L., Bian, Q., Ramnarine, E., Lonsdale, C. R., Alvarado, M. J., Kreidenweis, S. M.,
943   Jathar, S. H. & Pierce, J. R. (2019). More Than Emissions and Chemistry: Fire Size,
944   Dilution, and Background Aerosol Also Greatly Influence Near-Field Biomass Burning
945   Aerosol Aging. *Journal of Geophysical Research: Atmospheres*, *124*(10), 5589–5611.
946   https://doi.org/10.1029/2018JD029674

947   Ichoku, C., & Ellison, L. (2014). Global top-down smoke-aerosol emissions estimation using
948   satellite fire radiative power measurements. *Atmospheric Chemistry and Physics*, *14*(13),
949   6643–6667. https://doi.org/10.5194/acp-14-6643-2014

950 Ichoku, Charles, & Kaufman, Y. J. (2005). A method to derive smoke emission rates from
951   MODIS fire radiative energy measurements. *IEEE Transactions on Geoscience and Remote*
952   *Sensing*, *43*, 2636–2649. https://doi.org/10.1109/TGRS.2005.857328

953 Ichoku, Charles, Giglio, L., Wooster, M. J., & Remer, L. A. (2008). Global characterization of
954   biomass-burning patterns using satellite measurements of fire radiative energy. *Remote*
955   *Sensing of Environment*, *112*(6), 2950–2962. https://doi.org/10.1016/j.rse.2008.02.009

956 Kaiser, J. W., Flemming, J., Schultz, M. G., Suttie, M., & Wooster, M. J. (2009). *The MACC*
957   *Global Fire Assimilation System: First Emission Products (GFASv0)*. Retrieved from
958   http://www.ecmwf.int/publications/

959 Kaiser, J. W., Heil, A., Andreae, M. O., Benedetti, A., Chubarova, N., Jones, L., Morcrette, J. J.,
960   Razinger, M., Schultz, M. G., Suttie, M. & Van Der Werf, G. R. (2012). Biomass burning
961   emissions estimated with a global fire assimilation system based on observed fire radiative
962   power. *Biogeosciences*, *9*(1), 527–554. https://doi.org/10.5194/bg-9-527-2012

963 Keane, R. E., Herynk, J. M., Toney, C., Urbanski, S. P., Lutes, D. C. & Ottmar, R. D. (2013).
964   Evaluating the performance and mapping of three fuel classification systems using Forest
965   Inventory and Analysis surface fuel measurements. *Forest Ecology and Management*, *305*,
966   248-263. https://doi.org/10.1016/j.foreco.2013.06.001

967 Kennedy, M. C., Prichard, S. J., McKenzie, D., & French, N. H. F. (2020). Quantifying how
968   sources of uncertainty in combustible biomass propagate to prediction of wildland fire
969   emissions. *International Journal of Wildland Fire*, *29*(9), 793–806.
970   https://doi.org/10.1071/WF19160

971 Larkin, N. K., O'Neill, S. M., Solomon, R., Raffuse, S., Strand, T., Sullivan, D. C., Krull, C.,
972   Rorig, M., Peterson, J. & Ferguson, S. A. (2009). The BlueSky smoke modeling framework.
973   *International Journal of Wildland Fire*, *18*(8), 906–920. https://doi.org/10.1071/WF07086

974 Larkin, N. K., Raffuse, S. M., & Strand, T. M. (2014). Wildland fire emissions, carbon, and
975   climate: U.S. emissions inventories. *Forest Ecology and Management*, *317*, 61–69.
976   https://doi.org/10.1016/j.foreco.2013.09.012

977 Larsen, A. E., Reich, B. J., Ruminski, M., & Rappold, A. G. (2018). Impacts of fire smoke
978   plumes on regional air quality, 2006-2013. *Journal of Exposure Science and Environmental*
979   *Epidemiology*, *28*(4), 319-327. https://doi.org/10.1038/s41370-017-0013-x

980 Li, F., Val Martin, M., Andreae, M. O., Arneth, A., Hantson, S., Kaiser, J. W., Lasslop, G., Yue,
981   C., Bachelet, D., Forrest, M. & Kluzek, E. (2019). Historical (1700-2012) global multi-
982   model estimates of the fire emissions from the Fire Modeling Intercomparison Project
983   (FireMIP). *Atmospheric Chemistry and Physics*, *19*(19), 12545–12567.
984   https://doi.org/10.5194/acp-19-12545-2019

985 Liu, T., Mickley, L. J., Marlier, M. E., DeFries, R. S., Khan, M. F., Latif, M. T., & Karambelas,
986   A. (2020). Diagnosing spatial biases and uncertainties in global fire emissions inventories:
987   Indonesia as regional case study. *Remote Sensing of Environment*, *237*, 111557.

988   https://doi.org/10.1016/j.rse.2019.111557

989   Liu, Y. (2004). Variability of wildland fire emissions across the contiguous United States.
990   *Atmospheric Environment*, *38*(21), 3489–3499.
991   https://doi.org/10.1016/j.atmosenv.2004.02.004

992   May, A. A., McMeeking, G. R., Lee, T., Taylor, J. W., Craven, J. S., Burling, I., Sullivan, A. P.,
993   Akagi, S., Collett Jr., J. L., Flynn, M. & Coe, H. (2014). Aerosol emissions from prescribed
994   fires in the United States: A synthesis of laboratory and aircraft measurements. *Journal of*
995   *Geophysical Research: Atmospheres*, *119*(20), 11826–11849.
996   https://doi.org/10.1002/2014JD021848

997   McClure, C. D., Lim, C. Y., Hagan, D. H., Kroll, J. H., & Cappa, C. D. (2020). Biomass-
998   burning-derived particles from a wide variety of fuels - Part 1: Properties of primary
999   particles. *Atmospheric Chemistry and Physics*, *20*(3), 1531–1547.
1000   https://doi.org/10.5194/acp-20-1531-2020

1001   McKenzie, D., O'Neill, S. M., Larkin, N. K., & Norheim, R. A. (2006). Integrating models to
1002   predict regional haze from wildland fire. *Ecological Modelling*, *199*(3), 278–288.
1003   https://doi.org/10.1016/j.ecolmodel.2006.05.029

1004   McKenzie, D., French, N. H. F., & Ottmar, R. D. (2012). National database for calculating fuel
1005   available to wildfires. *Eos*, *Transactions American Geophysical Union*, *93*(6), 57–58.
1006   https://doi.org/10.1029/2012EO060002

1007   McMeeking, G. R., Kreidenweis, S. M., Baker, S., Carrico, C. M., Chow, J. C., Collett Jr., J. L.,
1008   Hao, W. M., Holden, A. S., Kirchstetter, T. W., Malm, W. C. & Moosmüller, H. (2009).
1009   Emissions of trace gases and aerosols during the open combustion of biomass in the
1010   laboratory. *Journal of Geophysical Research: Atmospheres*, *114*, D19210.
1011   https://doi.org/10.1029/2009JD011836

1012   Mell, W. E., Manzello, S. L., Maranghides, A., Butry, D., & Rehm, R. G. (2010). The wildland -
1013   urban interface fire problem - current approaches and research needs. *International Journal*
1014   *of Wildland Fire*, *19*(2), 238-251. https://doi.org/10.1071/WF07131

1015   Moore, R. H., Wiggins, E. B., Ahern, A. T., Zimmerman, S., Montgomery, L., Campuzano Jost,
1016   P., Robinson, C. E., Ziemba, L. D., Winstead, E. L., Anderson, B. E. & Brock, C.A . (2021).
1017   Sizing response of the Ultra-High Sensitivity Aerosol Spectrometer (UHSAS) and Laser
1018   Aerosol Spectrometer (LAS) to changes in submicron aerosol composition and refractive
1019   index. *Atmospheric Measurement Techniques*, *14*(6), 4517-4542.
1020   https://doi.org/10.5194/amt-14-4517-2021

1021   Mota, B., & Wooster, M. J. (2018). A new top-down approach for directly estimating biomass
1022   burning emissions and fuel consumption rates and totals from geostationary satellite fire
1023   radiative power (FRP). *Remote Sensing of Environment*, *206*, 45–62.
1024   https://doi.org/10.1016/j.rse.2017.12.016

1025   Nikonovas, T., North, P. R. J., & Doerr, S. H. (2017). Particulate emissions from large North

American wildfires estimated using a new top-down method. *Atmospheric Chemistry and Physics*, *17*(10), 6423–6438. https://doi.org/10.5194/acp-17-6423-2017

Noss, R. F., Franklin, J. F., Baker, W. L., Schoennagel, T., & Moyle, P. B. (2006). Managing fire-prone forests in the western United States. *Frontiers in Ecology and the Environment*, *4*(9), 481–487. https://doi.org/https://doi.org/10.1890/1540-9295(2006)4[481:MFFITW]2.0.CO;2

Ottmar, R. D., Sandberg, D. V., Riccardi, C. L., & Prichard, S. J. (2007). An overview of the Fuel Characteristic Classification System — Quantifying, classifying, and creating fuelbeds for resource planningThis article is one of a selection of papers published in the Special Forum on the Fuel Characteristic Classification System. *Canadian Journal of Forest Research*, *37*(12), 2383–2393. https://doi.org/10.1139/X07-077

Pan, X., Ichoku, C., Chin, M., Bian, H., Darmenov, A., Colarco, P., Ellison, L., Kucsera, T., Silva, A. D., Wang, J. & Oda, T. (2020). Six global biomass burning emission datasets: intercomparison and application in one global aerosol model. *Atmospheric Chemistry and Physics*, *20*(2), 969–994. https://doi.org/10.5194/acp-20-969-2020

Pettinari, M. L., & Chuvieco, E. (2016). Generation of a global fuel data set using the Fuel Characteristic Classification System. *Biogeosciences*, *13*(7), 2061–2076. https://doi.org/10.5194/bg-13-2061-2016

Prichard, S. J., Kennedy, M. C., Andreu, A. G., Eagle, P. C., French, N. H., & Billmire, M. (2019). Next-generation biomass mapping for regional emissions and carbon inventories: Incorporating uncertainty in wildland fuel characterization. *Journal of Geophysical Research: Biogeosciences, 124*(12)*, 3699-3716. https://doi.org/10.1071/WF19066.

Prichard, S. J., O'neill B, S. M., Eagle, P., Andreu, A. G., Drye, B., Dubowy, J., Urbanski, S., & Strand, T. (2020). Wildland fire emission factors in North America: synthesis of existing data, measurement needs and management applications. *International Journal of Wildland Fire*, *29*(2), 132–147. https://doi.org/10.1071/WF19066

Randerson, J. T., Chen, Y., Van Der Werf, G. R., Rogers, B. M., & Morton, D. C. (2012). Global burned area and biomass burning emissions from small fires. *Journal of Geophysical Research: Biogeosciences*, *117*, G04012. https://doi.org/10.1029/2012JG002128

Reid, J. S., Koppmann, R., Eck, T. F., & Eleuterio, D. P. (2005a). A review of biomass burning emissions part II: Intensive physical properties of biomass burning particles. *Atmospheric Chemistry and Physics*, *5*(3), 799-825. https://doi.org/10.5194/acp-5-799-2005

Reid, J.S., Eck, T.F., Christopher, S.A., Koppmann, R., Dubovik, O., Eleuterio, D.P., Holben, B.N., Reid, E.A. & Zhang, J. (2005b). A review of biomass burning emissions part III: Intensive optical properties of biomass burning particles. *Atmospheric Chemistry and Physics*, *5*(3), 827-849, https://doi.org/10.5194/acp-5-827-2005

Sachse, G. W., Collins, J. E. Jr., Hill, G. F., Wade, L. O., Burney, L. G., & Ritter, J. A. (1991). Airborne tunable diode laser sensor for high-precision concentration and flux measurements

1065   of carbon monoxide and methane. *Measurement of Atmospheric Gases*, *1433*, 157– 166.
1066   https://doi.org/10.1117/12.46162

1067   Sandberg, D. V., Ottmar, R. D., & Cushon, G. H. (2001). Characterizing fuels in the 21st
1068   Century. *International Journal of Wildland Fire*, *10*(4), 381–387.
1069   https://doi.org/10.1071/wf01036

1070   Santín, C., Doerr, S. H., Preston, C. M., & González-Rodríguez, G. (2015). Pyrogenic organic
1071   matter production from wildfires: a missing sink in the global carbon cycle. *Global Change*
1072   *Biology*, *21*(4), 1621–1633. https://doi.org/10.1111/gcb.12800

1073   Schmidt, C. (2019). Monitoring Fires with the GOES-R Series. In *The GOES-R Series: A New*
1074   *Generation of Geostationary Environmental Satellites* (pp. 145–163). Elsevier.
1075   https://doi.org/10.1016/B978-0-12-814327-8.00013-5

1076   Schultz, M. G., Heil, A., Hoelzemann, J. J., Spessa, A., Thonicke, K., Goldammer, J. G., Held,
1077   A. C., Pereira, J. M. & van Het Bolscher, M. (2008). Global wildland fire emissions from
1078   1960 to 2000. *Global Biogeochemical Cycles*, *22*, GB2002.
1079   https://doi.org/10.1029/2007GB003031

1080   Schweizer, D., Preisler, H. K., & Cisneros, R. (2018). Assessing relative differences in smoke
1081   exposure from prescribed, managed, and full suppression wildland fire. *Air Quality,*
1082   *Atmosphere & Health*, *12*(1), 87-95. https://doi.org/10.1007/s11869-018-0633-x

1083   Seiler, W., & Crutzen, P. J. (1980). Estimates of gross and net fluxes of carbon between the
1084   biosphere and the atmosphere from biomass burning. *Climatic Change*, *2*(3), 207–247.
1085   https://doi.org/10.1007/BF00137988

1086   Seinfeld, J. H., & Pandis, S. N. (2006). Interaction of Aerosols with Radiation. In *Atmospheric*
1087   *Chemistry and Physics: from Air Pollution to Climate Change* (pp. 691–719). Hoboken,
1088   New Jersey: John Wiley & Sons.

1089   Shingler, T., Crosbie, E., Ortega, A., Shiraiwa, M., Zuend, A., Beyersdorf, A., Ziemba, L.,
1090   Anderson, B., Thornhill, L., Perring, A. E., Schwarz, J. P., Campazano-Jost, P., Day, D. A.,
1091   Jimenez, J. L., Hair, J. W., Mikoviny, T., Wisthaler, A., & Sorooshian, A. (2016). Airborne
1092   Characterization of Sub-saturated Aerosol Hygroscopicity and Dry Refractive Index from
1093   the Surface to 6.5 km during the SEAC^{4}RS Campaign, *Journal Geophysical Research:*
1094   *Atmospheres*, *121*(8), 4188–4210. https://doi.org/10.1002/2015JD024498

1095   Stavros, E. N., Abatzoglou, J., Larkin, N. K., McKenzie, D., & Steel, E. A. (2014). Climate and
1096   very large wildland fires in the contiguous western USA. *International Journal of Wildland*
1097   *Fire*, *23*(7), 899-914. https://doi.org/10.1071/WF13169

1098   Stephens, S. L., & Ruth, L. W. (2005). Federal forest-fire policy in the United States. *Ecological*
1099   *Applications*, *15*(2), 532-542. https://doi.org/10.1890/04-0545

1100   Surawski, N. C., Sullivan, A. L., Roxburgh, S. H., Meyer, C. P. M., & Polglase, P. J. (2016).
1101   Incorrect interpretation of carbon mass balance biases global vegetation fire emission

1102   estimates. *Nature Communications*, *7*(1), 1–5. https://doi.org/10.1038/ncomms11536

1103   Susott, R. A., Ward, D. E., Babbitt, R. E., & Latham, D. J. (1991). The measurement of trace
1104   emissions and combustion characteristics for a mass fire In Levine, J. S. (Eds.), *Global*
1105   *Biomass Burning: Atmospheric, Climatic, and Biosphere Implications* (pp. 245-257).
1106   Cambridge, Massachusetts: The MIT Press.

1107   Susott, R. A., Olbu, G. J., Baker, S. P. & Ward, D. E. (1996). Carbon, Hydrogen, Nitrogen, and
1108   Thermogravimetric Analysis. In Levine, J. S. (Eds.), *Biomass Burning and Global Change:*
1109   *Remote sensing, Modeling and Inventory Development, and Biomass Burning in Africa*
1110   (Vol. 1, pp 249-259). Cambridge, Massachusetts: The MIT Press.

1111   Theobald, D. M., & Romme, W. H. (2007). Expansion of the US wildland-urban interface.
1112   *Landscape and Urban Planning*, *83*(4), 340–354.
1113   https://doi.org/10.1016/j.landurbplan.2007.06.002

1114   Urbanski, S. P., Hao, W. M., & Nordgren, B. (2011). The wildland fire emission inventory:
1115   Western United States emission estimates and an evaluation of uncertainty. *Atmospheric*
1116   *Chemistry and Physics*, *11*(24), 12973–13000. https://doi.org/10.5194/acp-11-12973-2011

1117   Ward, D. E., & Radke, L. F. (1993). Emissions measurements from vegetation fires: A
1118   comparative evaluation of methods and results. In P. J. Crutzen & J. G. Goldammer (Eds.),
1119   *Fire in the Environment: The Ecological, Atmosheric, and Climatic Importance of*
1120   *Vegetation Fires* (pp. 53–76). Chischester, England: John Wiley & Sons.

1121   Weaver, H. (1974). Effects of fire on temperate forests: western United States. In C. E.
1122   Kozlowski & T. T. Ahlgren (Eds.), *Fire and Ecosystems* (pp. 279–317). New York, New
1123   York: Academic Press.

1124   Van Der Werf, G. R., Randerson, J. T., Giglio, L., Van Leeuwen, T. T., Chen, Y., Rogers, B. M.,
1125   Mu, M., Van Marle, M. J., Morton, D. C., Collatz, G. J. & Yokelson, R.J. (2017). Global
1126   fire emissions estimates during 1997–2016. *Earth System Science Data*, *9*(2), 697–720.
1127   https://doi.org/10.5194/essd-9-697-2017

1128   van Leeuwen, T. T., van der Werf, G. R., Hoffmann, A. A., Detmers, R. G., Rücker, G., French,
1129   N. H. F., Archibald, S., Carvalho Jr., J. A., Cook, G. D., de Groot, W. J., Hély, C.,
1130   Kasischke, E. S., Kloster, S., McCarty, J. L., Pettinari, M. L., Savadogo, P., Alvarado, E. C.,
1131   Boschetti, L., Manuri, S., Meyer, C. P., Siegert, F., Trollope, L. A., & Trollope, W. S. W.
1132   (2014). Biomass burning fuel consumption rates: a field measurement database,
1133   *Biogeosciences*, *11*(24), 7305–7329, https://doi.org/10.5194/bg-11-7305-2014

1134   Vay, S. A., Woo, J. H., Anderson, B. E., Thornhill, K. L., Blake, D. R., Westberg, D. J., Kiley,
1135   C. M., Avery, M. A., Sachse, G. W., Streets, D. G., & Tsutsumi, Y. (2003). Influence of
1136   regional-scale anthropogenic emissions on CO_2 distributions over the western North
1137   Pacific. *Journal of Geophysical Research: Atmospheres*, *108*, 8801.
1138   https://doi.org/10.1029/2002JD003094

1139   Virkkula, A. (2010). Correction of the calibration of the 3-wavelength Particle Soot Absorption

1140   Photometer (3λ PSAP). *Aerosol Science and Technology*, *44*(8), 706-712.
1141   https://doi.org/10.1080/02786826.2010.482110

1142   Westerling, A. L., Gershunov, A., Brown, T. J., Cayan, D. R., & Dettinger, M. D. (2003).
1143   Climate and Wildfire in the Western United States. *Bulletin of the American Meteorological*
1144   *Society*, *84*(5), 595–604. https://doi.org/10.1175/BAMS-84-5-595

1145   Wiedinmyer, C., Akagi, S. K., Yokelson, R. J., Emmons, L. K., Al-Saadi, J. A., Orlando, J. J., &
1146   Soja, A. J. (2011). The Fire INventory from NCAR (FINN): A high resolution global model
1147   to estimate the emissions from open burning. *Geoscientific Model Development*, *4*(3), 625–
1148   641. https://doi.org/10.5194/gmd-4-625-2011

1149   Wiedinmyer, C., Quayle, B., Geron, C., Belote, A., McKenzie, D., Zhang, X., O'Neill, S. &
1150   Wynne, K. K. (2006). Estimating emissions from fires in North America for air quality
1151   modeling. *Atmospheric Environment*, *40*(19), 3419–3432.
1152   https://doi.org/10.1016/j.atmosenv.2006.02.010

1153   Wiggins, E. B., Soja, A. J., Gargulinski, E., Halliday, H. S., Pierce, R. B., Schmidt, C. C.,
1154   Nowak, J. B., DiGangi, J. P., Diskin, G. S., Katich, J. M. & Perring, A. E. (2020). High
1155   Temporal Resolution Satellite Observations of Fire Radiative Power Reveal Link Between
1156   Fire Behavior and Aerosol and Gas Emissions. *Geophysical Research Letters*, *47*(23),
1157   e2020GL090707. https://doi.org/10.1029/2020GL090707

1158   Wiggins, E. B., Andrews, A., Sweeney, C., Miller, J. B., Miller, C. E., Veraverbeke, S.,
1159   Commane, R., Wofsy, S., Henderson, J. M. & Randerson, J. T. (2021). Boreal forest fire
1160   CO and CH_4 emission factors derived from tower observations in Alaska during the extreme
1161   fire season of 2015. *Atmospheric Chemistry and Physics*, *21*(11), 8557–8574.
1162   https://doi.org/10.5194/acp-21-8557-2021

1163   Wooster, M. J., Roberts, G., Perry, G. L. W., & Kaufman, Y. J. (2005). Retrieval of biomass
1164   combustion rates and totals from fire radiative power observations: FRP derivation and
1165   calibration relationships between biomass consumption and fire radiative energy release.
1166   *Journal of Geophysical Research: Atmospheres*, *110*(24), 1–24.
1167   https://doi.org/10.1029/2005JD006318

1168   Xu, W., Wooster, M. J., He, J., & Zhang, T. (2021). Improvements in high-temporal resolution
1169   active fire detection and FRP retrieval over the Americas using GOES-16 ABI with the
1170   geostationary Fire Thermal Anomaly (FTA) algorithm. *Science of Remote Sensing*, *3*,
1171   100016. https://doi.org/10.1016/j.srs.2021.100016

1172   Yokelson, R.J., Griffith, D.W. & Ward, D.E., 1996. Open-path Fourier transform infrared studies
1173   of large-scale laboratory biomass fires. J*ournal of Geophysical Research: Atmospheres*,
1174   *101*(D15), 21067-21080. https://doi.org/10.1029/96JD01800

1175   Yokelson, Robert J., Susott, R., Ward, D. E., Reardon, J., & Griffith, D. W. T. (1997). Emissions
1176   from smoldering combustion of biomass measured by open-path Fourier transform infrared
1177   spectroscopy. *Journal of Geophysical Research: Atmospheres*, *102*(15), 18865–18877.
1178   https://doi.org/10.1029/97jd00852

1179 Yokelson, R. J., Goode, J. G., Ward, D. E., Susott, R. A., Babbitt, R. E., Wade, D. D., Bertschi,
1180   I., Griffith, D. W. & Hao, W. M. (1999). Emissions of formaldehyde, acetic acid, methanol,
1181   and other trace gases from biomass fires in North Carolina measured by airborne Fourier
1182   transform infrared spectroscopy. *Journal of Geophysical Research: Atmospheres*,
1183   *104*(D23), 30109–30125. https://doi.org/10.1029/1999JD900817

1184 Yokelson, R. J., Burling, I. R., Gilman, J. B., Warneke, C., Stockwell, C. E., Gouw, J. D., Akagi,
1185   S. K., Urbanski, S. P., Veres, P., Roberts, J. M. & Kuster, W. C. (2013). Coupling field and
1186   laboratory measurements to estimate the emission factors of identified and unidentified
1187   trace gases for prescribed fires. *Atmospheric Chemistry and Phys*ics, *13*(1), 89–116.
1188   https://doi.org/10.5194/acp-13-89-2013

1189

1190 **Figures and Tables**
1191
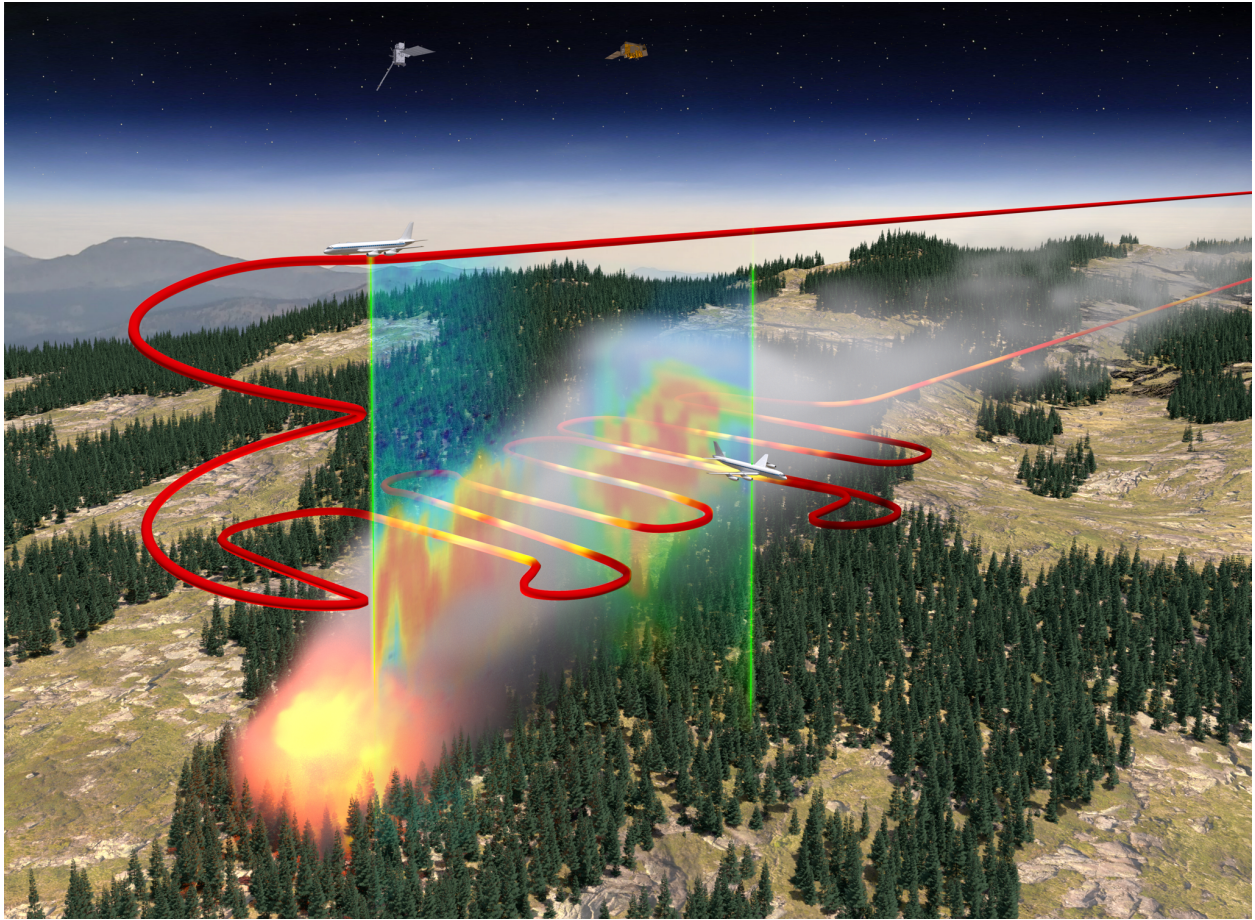
1192
1193
1194 **Figure 1.** Conceptual image of a typical wildland fire and smoke plume observed during FIREX-
1195 AQ as well as the observational platforms and analysis approaches. The DC-8 flight track is
1196 given in red and colored by in situ particle concentrations for the cross-sectional legs. As
1197 described in the text, the DC-8 initially completes a longitudinal run where the nadir HSRL
1198 measurement provides the full smoke curtain below the aircraft, which is then followed by a
1199 series of successively downwind flight legs where the nadir- and zenith-pointing HSRL curtains
1200 are used to contextualize the cross-sectional, in situ measurements. Image credit: NASA / Tim
1201 Marvel.
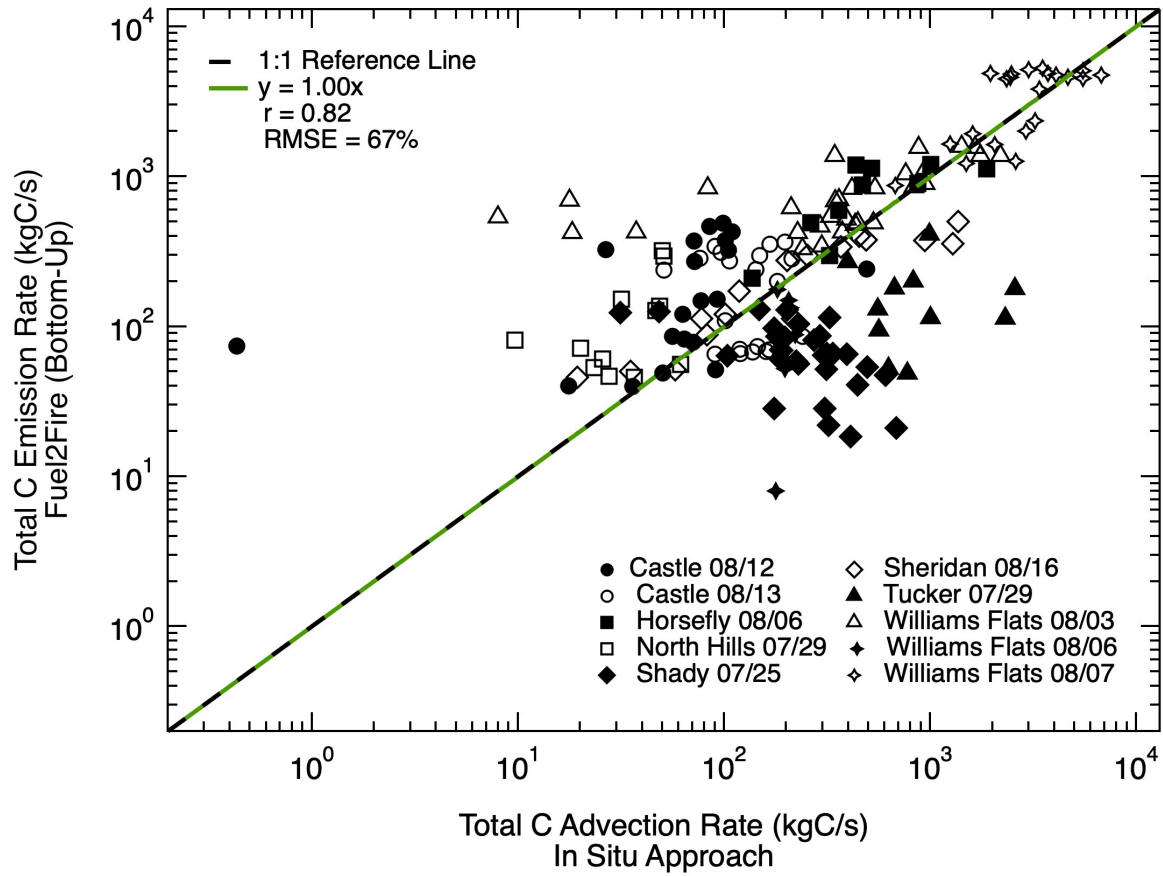
Figure 2. Relationship between total carbon emission rates (E_C) from the high resolution bottom-up approach, Fuel2Fire, and the in situ approach. Different markers correspond to specific fires and repeated markers correspond to different transects of the same fire. The green line shows the fit between E_C using a reduced major axis regression with a forced zero intercept. The dashed black line shows a perfect 1:1 relationship for reference. The slope for the linear fit, Pearson's correlation coefficient (r), and root mean square error (RMSE) is given in the legend.
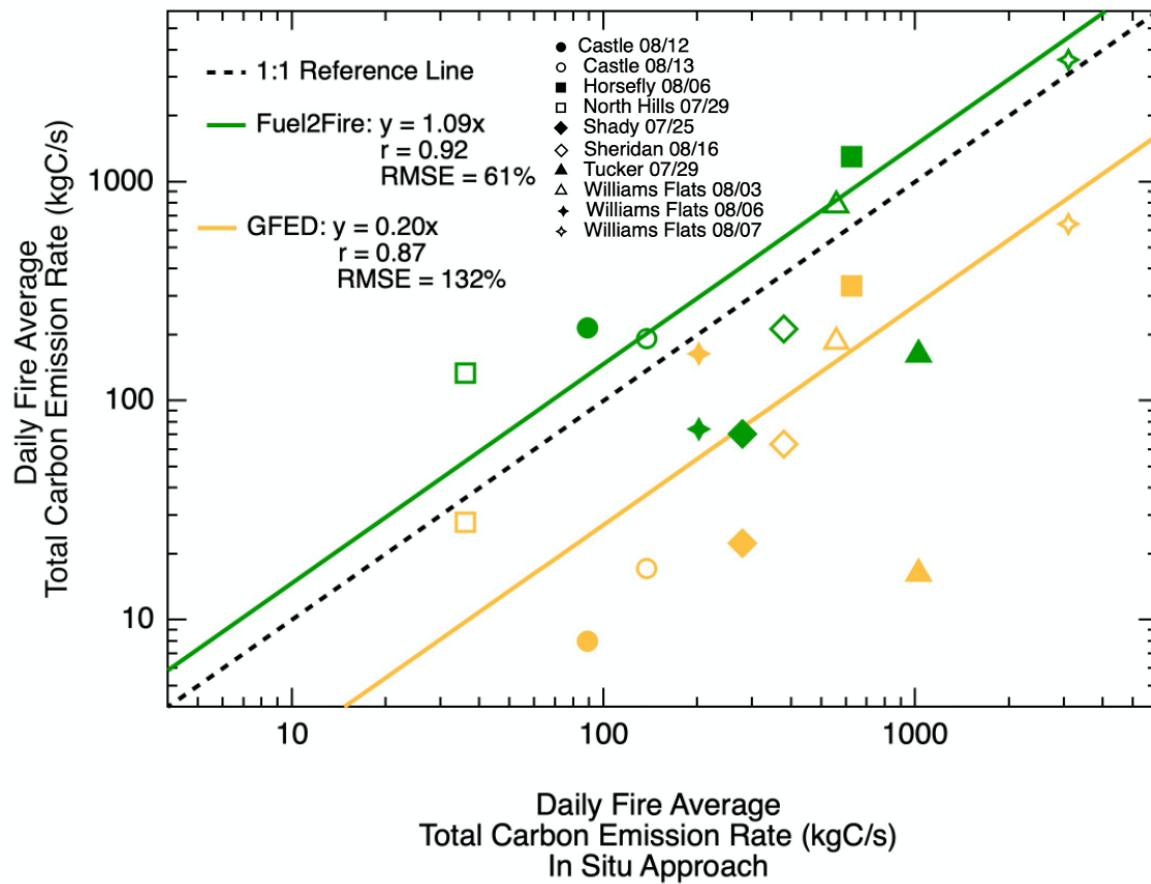
1210

**Figure 3.** Relationship between daily fire average total carbon emission rates (E_C) from Fuel2Fire and GFED versus the in situ measurement based approach. Different markers correspond to specific fires. The green line shows the fit between Fuel2Fire E_C estimates versus the in situ approach using a reduced major axis regression with a forced zero intercept. The yellow line shows the fit between GFED E_C estimates versus the in situ approach. The dashed black line shows a perfect 1:1 relationship for reference. The slope for the linear fit, Pearson's correlation coefficient (r), and root mean square error (RMSE) is given in the legend.

1218
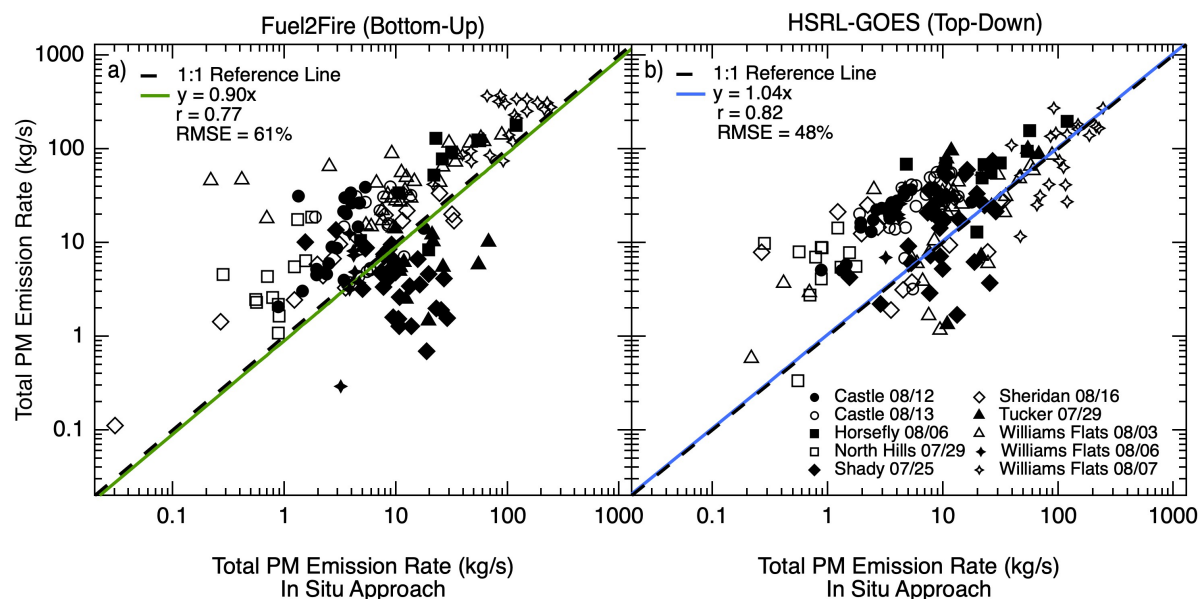
Figure 4. Relationship between total PM emission rates (E_{PM}) derived from the high-resolution bottom-up approach (Fuel2Fire) versus in situ shown in panel a, and the same relationship between the high resolution top-down aircraft approach (HSRL-GOES) and the in situ approach shown in panel b. The green line shows the reduced major axis regression with a forced zero intercept for Fuel2Fire E_{PM} estimates versus in situ, and the blue line shows the fit for the HSRL-GOES E_{PM} estimates versus in situ. Legend gives the slope for the linear fit, Pearson's correlation coefficient (r), and root mean square error (RMSE).

1227
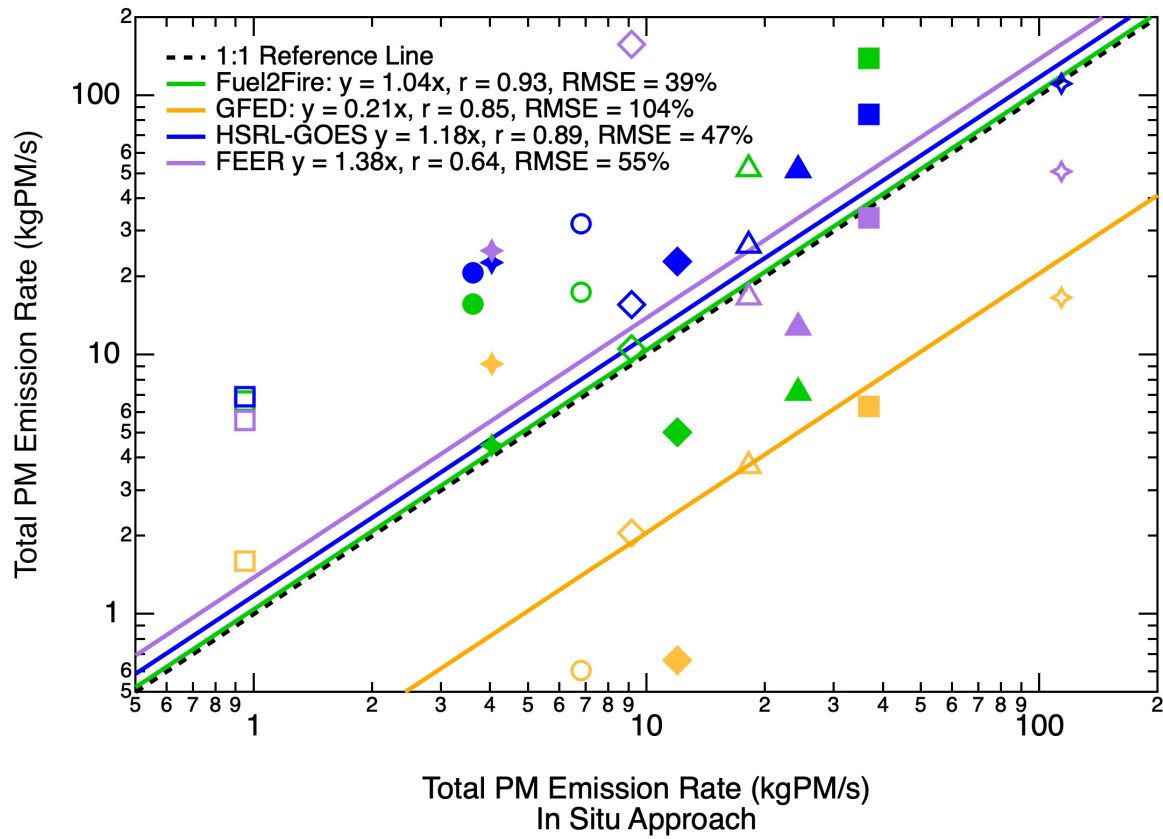
Figure 5. Daily fire average PM emission rates (E_{PM}) from Fuel2Fire, HSRL-GOES, GFED, and FEER compared to estimates from the in situ approach. Green markers represent estimates from Fuel2Fire and the green line represents the reduced major axis regression with a forced zero intercept between Fuel2Fire estimates and in situ estimates. Blue markers and line represent HSRL-GOES estimates and regression. Purple markers and line represent FEER estimates and regression. Orange markers and line represent GFED estimates and regression. The slope for the linear fit, Pearson's correlation coefficient (r), and root mean square error (RMSE) is given in the legend.

1236

1237
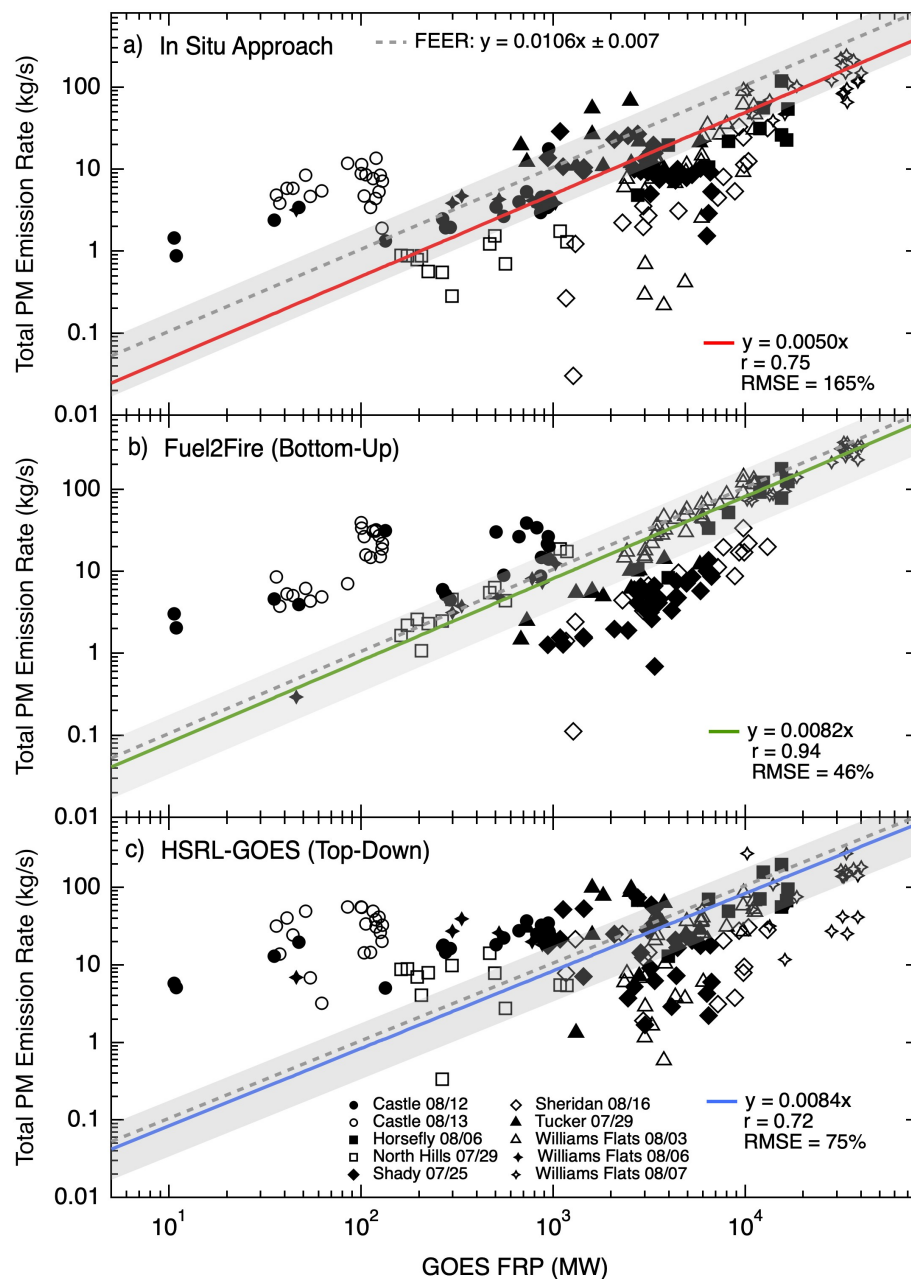
1238

Figure 6. Relationship between GOES FRP and total PM emission rates (E_{PM}) derived from the in situ approach (panel a) and the same relationship for Fuel2Fire (panel b) and HSRL-GOES (panel c). The red line shows the fit to a reduced major axis regression with a forced zero intercept for the GOES FRP versus in situ comparison, the green line shows the fit for Fuel2Fire, and the blue line shows the fit for HSRL-GOES. The slope of each regression is equal to the smoke emission coefficient (C_e). The dashed grey line is the C_e derived from FEER and the grey shading represents the corresponding uncertainty range. Legend gives the slope for the linear fit, correlation coefficient (r), and root mean square error (RMSE %).

1247

1248
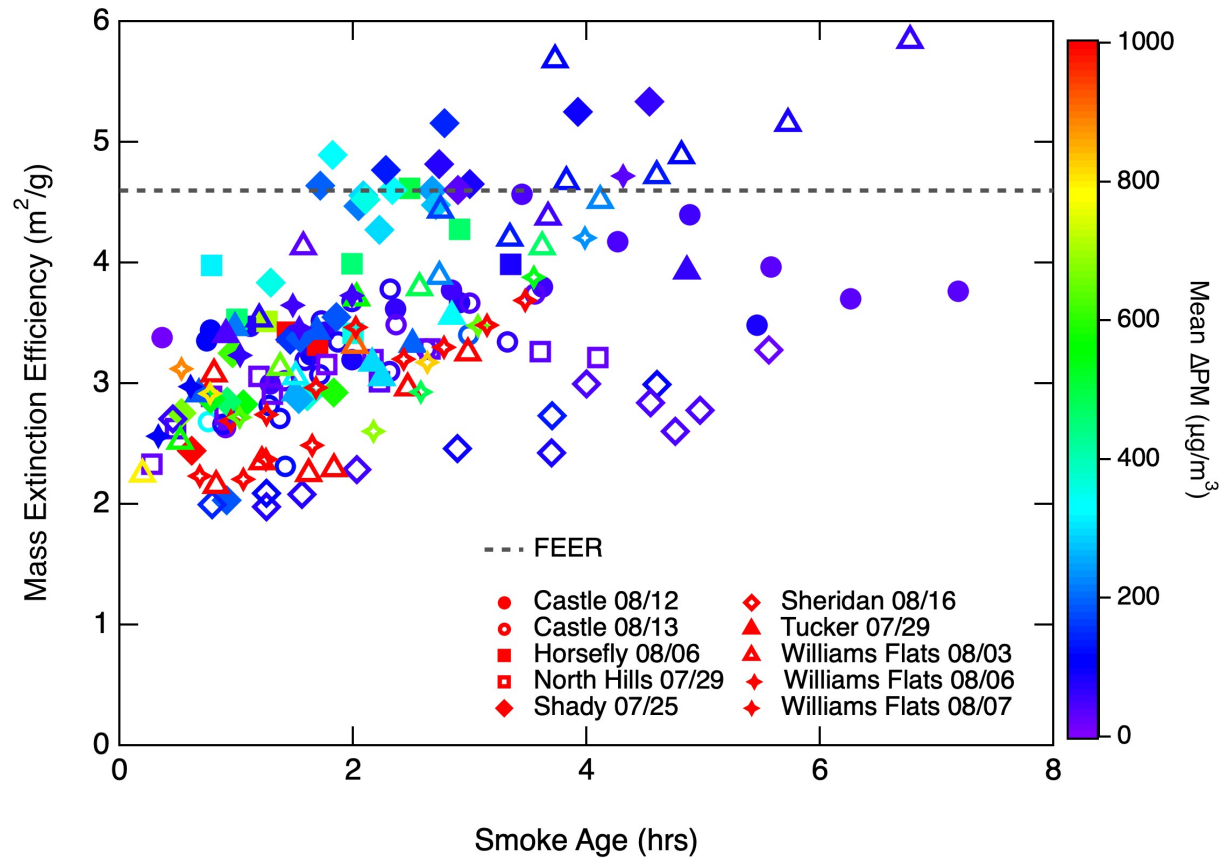
Figure 7. Mass extinction efficiency (MEE) versus smoke age per transect for each fire. Markers
are colored as a function of transect mean excess PM concentration. The constant MEE assumed
by FEER is shown as the dashed black line for reference.

1249
1250
1251

1252

1253

Inventory or Approach	Style	Spatial Range	Temporal Resolution	Eqns.	Input Variables	Output Variables
GFED4.1s	Bottom-up	Global	Daily	1	BA, FL, CC, F_C	E_C
				2	$\hat{E}_{C_{GFED}}$, EF_{PM}, F_c, ΔX_{GFED}	E_{PM}
FEERv1.0	Top-down	Global	Daily	3	C_e (MODIS), FRP (MODIS)	E_{PM}
				4	$\hat{E}_{PM_{FEER}}$, ΔX_{FEER}	E_{PM}
In Situ	In situ	Western US (FIREX-AQ)	Sub-plume timescale (per aircraft transect)	5	CO_2, CO, CH_4, OC, BC, PM, H, WS, GS	E_C, E_{PM}
				6	Δz, β	H
Fuel2Fire	Bottom-up	Western US (FIREX-AQ)	Sub-plume timescale (per aircraft transect)	1	BA, FL, CC, F_C	E_C
				7	E_C, EF_{PM}, F_C	E_{PM}
HSRL-GOES	Top-down	Western US (FIREX-AQ)	Sub-plume timescale (per aircraft transect)	3	C_e (Aircraft-GOES), FRP (GOES)	E_{PM}
				8	WS, GS, MEE, FRP (GOES), AOT	C_e
				9	α_t, Δz	AOT

1254 **Table 1.** Summary of approaches used to calculate fire carbon and PM emission rates. Note
1255 GFED4.1s also provides data at a 3hr temporal resolution, but we use only the daily product.

1256

		Fuel2Fire E_{PM}			HSRL-GOES E_{PM}		
Fire Name	Date Flown	m	r	RMSE	m	r	RMSE
Shady	07/25	0.13	0.44	13%	1.69	0.53	67%
North Hills	07/29	1.69	0.45	58%	6.27	0.55	30%
Tucker	07/29	0.10	0.61	39%	1.59	0.66	107%
Williams Flats	08/03	1.13	0.89	15%	1.07	0.84	149%
Williams Flats	08/06	0.59	0.07	116%	5.76	0.33	37%
Horsefly	08/06	1.70	0.63	627%	1.92	0.89	15%
Williams Flats	08/07	0.88	0.63	45%	0.94	0.69	87%
Castle	08/12	1.10	0.56	29%	3.54	0.73	18%
Castle	08/13	1.15	0.53	232%	4.48	0.71	232%
Sheridan	08/16	0.41	0.77	1529%	0.93	0.69	276%

1257 **Table 2.** Reduced major axis regression slope (m), Pearson's correlation coefficient (r), and root
1258 mean square error (RMSE) for PM emission rates (E_{PM}) from Fuel2Fire and HSRL-GOES versus
1259 the in situ based approach per fire. Fire name is given in the far left panel, followed by date
1260 flown.

1261

		In Situ			Fuel2Fire			HSRL-GOES		
Fire Name	Date Flown	m	r	RMSE	m	r	RMSE	m	r	RMSE
Shady	07/25	0.0022	0.53	85%	0.001	0.80	148%	0.012	0.44	78%
North Hills	07/29	0.0011	0.77	57%	0.014	0.95	46%	0.015	0.61	40%
Tucker	07/29	0.0076	0.49	74%	0.003	0.89	55%	0.033	0.60	63%
Williams Flats	08/03	0.0039	0.69	934%	0.010	0.91	71%	0.011	0.69	139%
Williams Flats	08/06	0.0039	0.70	6%	0.010	0.96	491%	0.057	0.63	69%
Horsefly	08/06	0.0012	0.61	292%	0.008	0.84	311%	0.012	0.69	118%
Williams Flats	08/07	0.0040	0.67	21%	0.009	0.90	1%	0.008	0.45	18%
Castle	08/12	0.0060	0.58	4531%	0.027	0.68	209%	0.060	0.86	111%
Castle	08/13	0.0646	0.61	57%	0.204	0.65	147%	0.555	0.55	81%
Sheridan	08/16	0.0017	0.68	3154%	0.002	0.84	1199%	0.005	0.66	274%

1262 **Table 3.** Reduced major axis regression slope (m), Pearson's correlation coefficient (r), and root
1263 mean square error (RMSE) for GOES FRP versus total PM emission rates (E_{PM}) for the in situ
1264 approach, Fuel2Fire, and HSRL-GOES per individual fire. The slope is equal to the smoke
1265 emission coefficient (C_e).

1266

Reconciling Assumptions in Bottom-up and Top-down Approaches for Estimating Aerosol Emission Rates from Wildland Fires using Observations from FIREX-AQ

E. B. Wiggins[1,2], B. E. Anderson[2], M. D. Brown[2,3], P. Campuzano-Jost[4], G. Chen[2], J. Crawford[2], E. C. Crosbie[2,3], J. Dibb[5], J. P. DiGangi[2], G. S. Diskin[2], M. Fenn[2,3], F. Gallo[1,2], E. Gargulinski[6], H. Guo[4], J. W. Hair[2], H. S. Halliday[7], C. Ichoku[8], J. L. Jimenez[4], C. E. Jordan[2,6], J. M. Katich[4,9], J. B. Nowak[2], A. E. Perring[10], C. E. Robinson[2,3], K. J. Sanchez[1,2], M. Schueneman[4], J. P. Schwarz[9], T. J. Shingler[2], M. A. Shook[2], A. Soja[2,6], C. E. Stockwell[4,9], K. L. Thornhill[2,3], K. R. Travis[2], C. Warneke[9], E. L. Winstead[2,3], L. D. Ziemba[2], and R. H. Moore[2]

[1]NASA Postdoctoral Program, Universities Space Research Association, Columbia, MD

[2]NASA Langley Research Center, Hampton, VA

[3]Science Systems and Applications, Inc., Hampton, VA

[4]CIRES, University of Colorado Boulder, Boulder, CO, USA

[5]Earth Systems Research Center, University of New Hampshire, NH, USA

[6]National Institute of Aerospace, Hampton, VA

[7]Environmental Protection Agency, Research Triangle, NC, USA

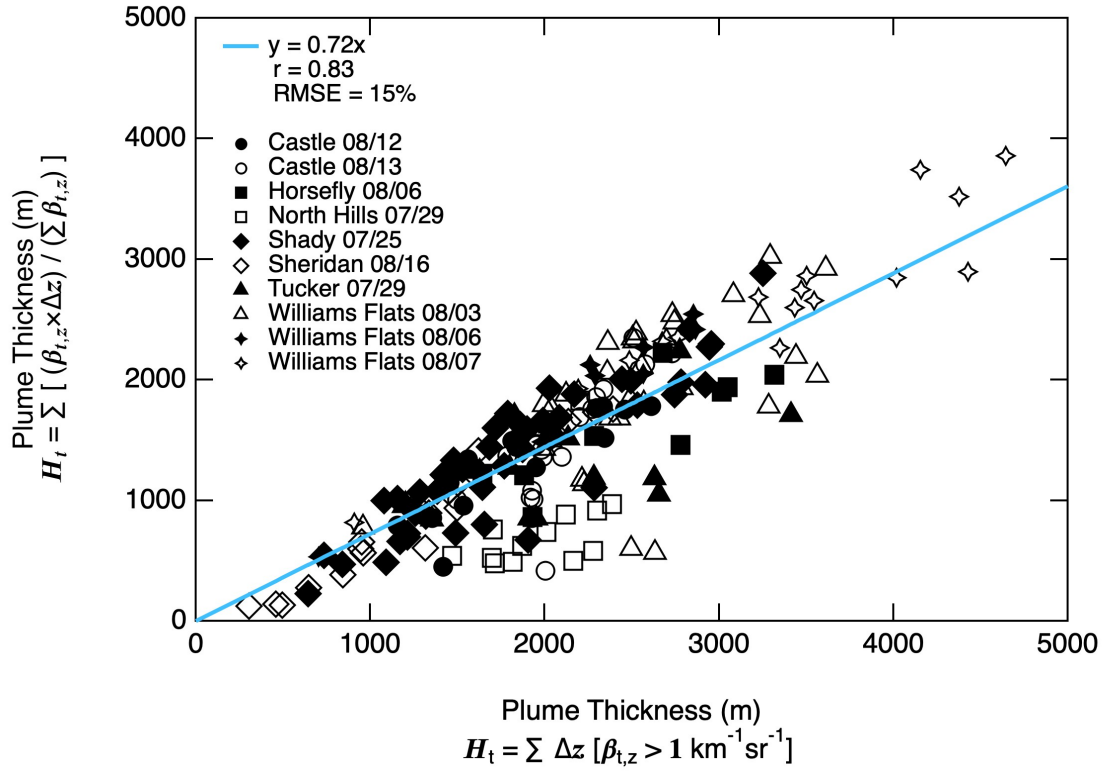[8]College of Arts and Sciences, Howard University, Washington, DC, USA

[9]NOAA Chemical Science Laboratory, Boulder, CO, USA

[10]Department of Chemistry, Colgate University, Hamilton, NY, USA

Contents of this file

Figure S1. Relationship between two different methods to calculate plume thickness per transect for each fire. X-axis shows plume thickness calculated using equation 6 and y-axis shows plume thickness calculated as a function of the backscatter coefficient distribution throughout the HSRL curtain. Blue line shows the fit to a reduced major axis regression with a forced zero intercept. Pearson's correlation coefficient (r) and root mean square error (RMSE) are given in the legend.
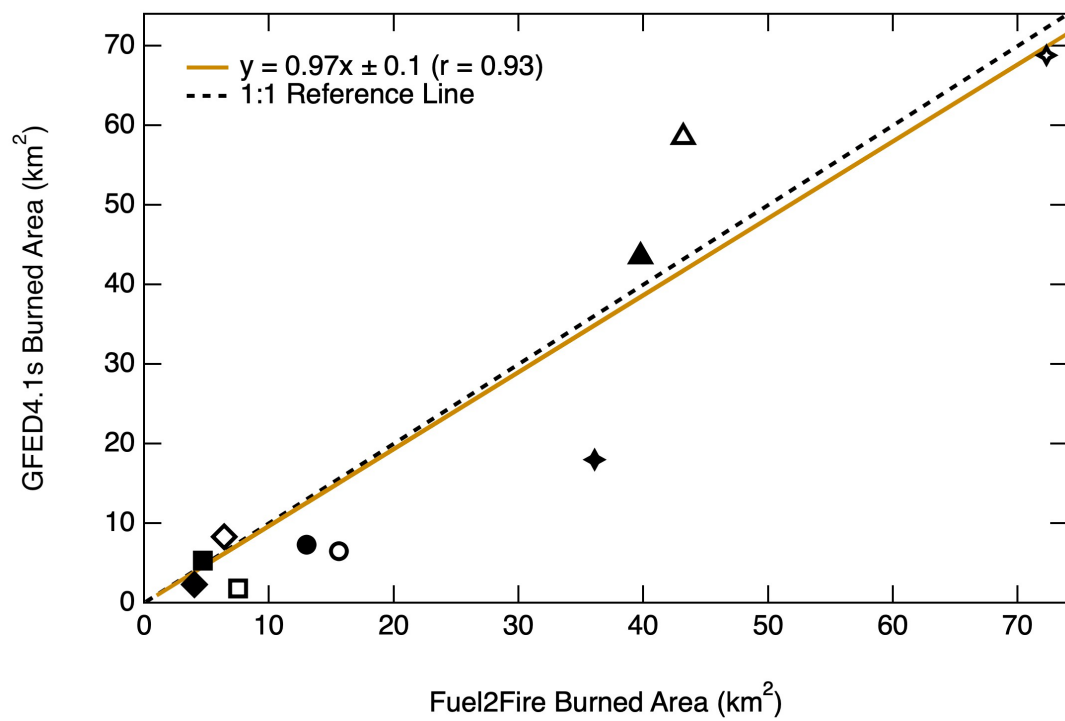
Figure S2. Total daily burned area per fire from Fuel2Fire versus GFED4.1s. The brown line shows the fit to a reduced major axis regression with a forced zero intercept. The slope and correlation coefficient are given in the legend. The black dashed line shows a perfect 1:1 relationship for reference.
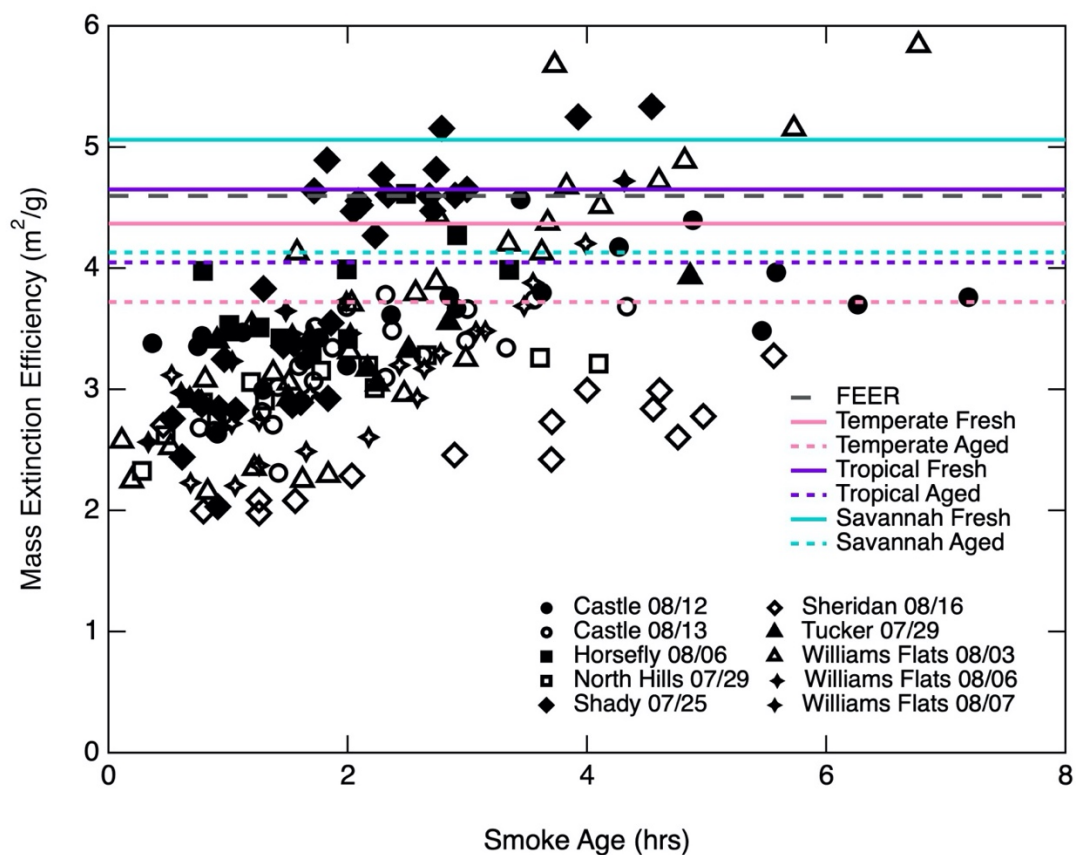
Figure S3. Mass extinction efficiency (MEE) calculated using in situ aircraft measurements for each fire per transect versus smoke age. Colored lines represent ecosystem average mass extinction efficiency for biomass burning particles taken from Reid et al. (2005b). Solid lines show MEE from fresh smoke (less than one day old) and dashed lines show MEE calculated using aged smoke (older than one day). The assumed MEE used by FEER is shown as the black dashed line.
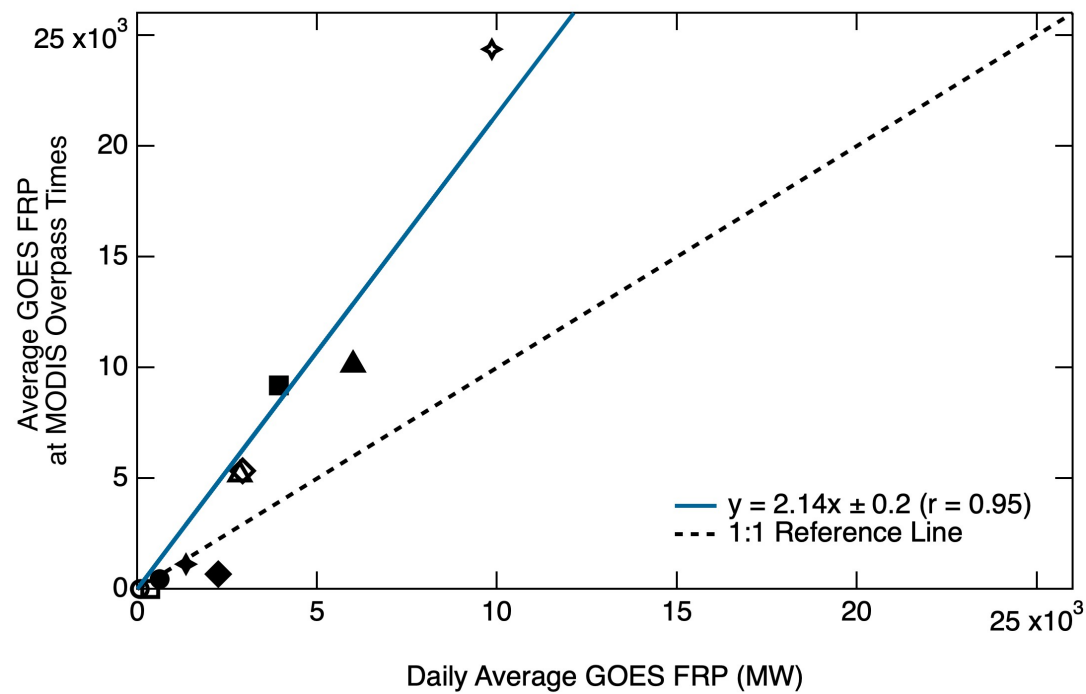
Figure S4. Daily average GOES FRP observations per fire versus average GOES FRP observations within 30 mins of the overpass times for MODIS onboard both Aqua and Terra per fire. The teal line shows reduced major axis regression line with the slope and correlation coefficient given in the legend. The black dashed line shows a perfect 1:1 relationship for reference.

Approach	Variable Relative Error			$\mu \pm \sigma$	IQR	Reference
GFED	$\delta E_{PM} = 126\%$	$\delta E_C = 120\%$	$\delta BA = 44\%$	-	-	Giglio et al. (2018)
			$\delta FL = 111\%$	75 ± 83	130	Van Leeuwen et al. (2014)
			$\delta CC = 11\%$	79 ± 9	14.0	Van Leeuwen et al. (2014)
			$\delta FC = 10\%$	500 ± 5	-	Akagi et al. (2011)
		$\delta EF_{PM} = 36\%$		17.6 ± 6.4	7	van der Werf et al. (2017)
FEER	$\delta E_{PM} = 78\%$	$\delta C_e = 73\%$		0.011 ± 0.008	0.008	Ichoku and Ellison (2014)
		$\delta FRP = 27\%$		-	-	Freeborn et al. (2014)
In Situ	$\delta E_C = 66\%$ $\delta E_{PM} = 75\%$	$\delta WS = 17\%$		6 ± 1	4	FIREX-AQ Observations
		$\delta GS = 3\%$		154 ± 5	16	
		$\delta Ht = 28\%$		2121 ± 594	593	
		$\delta \Delta C = 56\%$		0.009 ± 0.005	0.009	
		$\delta \Delta PM = 67\%$		0.0006 ± 0.0004	0.001	
Fuel2Fire	$\delta E_{PM} = 67\%$	$\delta E_C = 55\%$		1322 ± 729	510	Fuel2Fire (Internal)
		$\delta EF_{PM} = 38\%$		16 ± 6	7	FIREX-AQ Observations
HSRL-GOES	$\delta E_{PM} = 78\%$	$\delta C_e = 67\%$		0.006 ± 0.004	0.005	FIREX-AQ Observations
		$\delta FRP = 40\%$		-	-	Li et al. (2020)

Table S1. Relative uncertainty (δ) given as a percentage for E_{PM} and E_C (when available) derived using GFED, FEER, in situ measurements, Fuel2Fire, and HSRL-GOES. From left to right the dependent variables are broken down into the individual independent variables required for their calculation. Relative uncertainty for each independent variable is calculated as the standard deviation (σ) divided by the mean (μ), and relative uncertainty for each dependent variable is computed by error propagation through the equation by which they are defined. If the mean and standard deviation are not available, the relative uncertainty for a variable is taken directly from the corresponding reference. Mean, standard deviation, and interquartile range (IQR) are derived from aircraft observations during smoke plume transects and averaged over all the Western US wildland fires included in this study or calculated based on data from previous studies when available.